LOW-RESOURCE DIAGNOSTIC ASSAY BASED ON DISRUPTION OF RADIAL

FLOW IN AN EVAPORATING DROP

By

Joshua R. Trantum

Thesis

Submitted to the Faculty of the

Graduate School of Vanderbilt University

in partial fulfillment of the requirements

for the degree of

MASTER OF SCIENCE

in

Biomedical Engineering

December, 2010

Nashville, Tennessee

Approved:

Professor Frederick R. Haselton

Professor David W. Wright

To my grandfather, Dr. Robert C. Erwin

ACKNOWLEDGEMENTS

LIST OF TABLES

LIST OF FIGURES

TABLE OF CONTENTS

CHAPTER I

INTRODUCTION

Low-Resource Diagnostics

The leading causes of mortality in emerging nations versus developed nations are highly dichotomous. Ischemic heart disease, cerebrovascular disease, and cancer are dominant causes of mortality in developed countries [3]. By contrast, more than 95% of all deaths in low-income countries are attributed to infectious diseases (e.g. acute respiratory infections, HIV, TB, and malaria) [4]. Income disparity has resulted in dilapidated and deficient infrastructure, scarce resources, and a sub-par average education level. These conditions hinder preventive measures, early and accurate diagnosis, and the distribution and administration of effective therapy. The largest infectious disease burden is concentrated in Sub-Saharan Africa; where in 2006 malaria alone caused 709,000 deaths [5]. Disease is often treated symptomatically based on local disease prevalence [6]. This approach, tacitly approved by the World Health Organization absent sufficient alternatives, poses several drawbacks. Treatment is often delayed encumbering efforts to contain the spread of a contagious pathogen. Drugs erroneously prescribed to misdiagnosed patients accelerates the development of drug-resistant pathogens decreasing the lifetime effectiveness of a given therapeutic. The increasing sophistication with which next generation drugs must be designed significantly contributes to overall cost of therapy. Moreover, misdiagnosis increases the chance of a patient succumbing to an otherwise treatable disease. Early and accurate disease detection thus represents a

1

significant opportunity for improved patient outcomes and reduced cost to an already economically burdened population.

Effective point-of-care (POC) diagnostic strategies must consider the paucity of medical resources, including facilities, instrumentation, and trained personnel, in addition to potentially harsh storage and operating conditions. State-of-the art facilities and testing protocols do exist in the urban centers of Sub-Saharan Africa, however they remain capacity constrained. Early and accurate disease detection is most beneficially deployed at the front-line of infection – that is to say the remote village or town. In this setting the operator is most likely not a trained medical professional. Under these conditions an effective point-of-care diagnostic must be low-cost, intuitive, and require minimal-to-no instrumentation for sample processing and test interpretation. The assay must also be sufficiently robust to withstand long and harsh storage conditions and to generate repeatable results in a sub-optimal operating setting. Over the last two decades much progress has been made toward the design and distribution of POC diagnostics for low-resource regions [6]. However, currently available POC diagnostics fall short of meeting the requirements necessary for effective and reliable detection of malaria, the leading cause of death in Sub-Saharan Africa [7-10].

Malaria

The World Health Organization estimates approximately 250 million cases of malaria in 2006 causing 881,000 deaths [11]. The disease is responsible for one in five childhood deaths in Sub-Saharan Africa [11, 12]. Standard of care treatment has changed over the last decade as the parasite that causes the disease has gained resistance to the most commonly prescribed therapeutic, chloroquine [13]. A new group of fast-acting anti-malarial drugs, known as artemisinin-based combination therapies, (ACT) have shown to be effective [14]. However the high cost of the newer anti-malarials has placed an enormous economic burden on the low-income countries of Sub-Saharan Africa with as much as 40% of healthcare spending attributed to fighting malarial infections [11]. The World Health Organization estimates the malaria economic burden to be ~1.3% gross domestic product in severely affected countries [11].

Malaria is caused by any one of four different types of protozoan parasites belonging to the genus Plasmodium. The most prevalent malaria-causing species of the genus is *P. falciparum*. The parasite life cycle is divided between the mosquito vector and human host. The parasite initially exists as gametocytes in the mosquito vector, which mature into sporozoites. During feeding, sporozoites are transferred to the human host where they rapidly accumulate in the liver. Within one to two weeks, the sporozoites develop into schizonts, which eventually rupture releasing thousands of merozoites into the blood stream. The merozoites invade red blood cells where they reproduce until the cells lyse freeing the progeny to invade surrounding red blood cells. As this cycle continues malaria symptoms emerge and intensify, typically appearing 6-14 days following initial infection. Some merozoites differentiate into gametocytes, which are transported to a

mosquito vector during feeding thereby perpetuating the parasite life cycle and propagating the disease. Malaria exists at pandemic proportions in the tropical climates that are most conducive to mosquito infestations. Wealthier nations have successfully eradicated malaria by deploying mosquito containment strategies combined with effective anti-malarial therapies. However, lower-income and less advanced countries incapable of such prophylactic measures remain highly vulnerable to the disease. Moreover the economic burden imparted on highly infected regions represents a positive feedback mechanism in which therapeutic costs absorb the scarce capital resources that could otherwise be used for preventative measures. A low-cost, early, and accurate diagnosis is an essential component of an effective anti-malaria campaign.

The complex parasite life cycle creates a challenge for both diagnosis and therapy. As the parasite progresses between development stages, the antigen expression profile also changes. Therefore, available biomarkers used by diagnostic or therapeutic approaches are also life cycle stage dependent. At the sporozoite stage, the parasite coat consists mainly of circumsporozoite protein (CS). Red blood cells infected with merozoites express merozoite surface antigen, MSA-1 and MSA-2, in addition to ring-infected erythrocyte surface antigen, RESA. A biomarker commonly used in diagnostic assays is histidine-rich protein, a soluble protein secreted by merozoites. The protein is secreted only by *P. Falciparum* and is known as *pfHRP2*. Merozoites secrete *pfHRP2* in high copy number, sometimes reaching 10^{10} molecules per µL serum depending on the degree of parasitemia.

The gold standard for diagnosing malaria is to count the number of parasites per unit volume of sample in a thick film or thin blood smear under microscopy. The limit of

detection using thick film microscopy is ~ 5-20 parasites per μL [15]. However, this technique requires a trained microscopist, a microscope, and conditions conducive to sample handling, preparation, and storage. Thick or thin smear microscopy is therefore not well suited for point-of-care testing. Other methods have been shown to be effective, such as fluorescence staining, amperometric immunosensing, polymerase chain reaction, and ELISA [15-17]. However, these all suffer from the same shortcomings as microscopy with respect to a low-resource testing environment. Development of rapid diagnostic tests (RDTs) in recent years has successfully circumvented many of the challenges facing the traditional approaches for the point-of-care setting. RDTs have a limit of detection of ~ 100 parasites per μL [15, 18]. In the hospital setting, RDTs have been shown to operate with 95.4% sensitivity and 95.9% specificity [19].

Lateral Flow Assay

The most common type of RDT deployed for malaria POC testing is the lateral flow assay (LFA), also known as the immunochromatographic device. An LFA generally consists of four components: a sample pad, conjugate pad, nitrocellulose membrane, and absorbent pad. These layers are laminated to a plastic backing. The device uses capillary action to drive the sample fluid down a test strip where the sample is exposed to antibodies immobilized in specific regions on the nitrocellulose. LFAs designed to detect malaria follow a sandwich strategy analogous to an ELISA test (Figure 1). The sample first encounters a labeling agent in the conjugate pad. If the antigen is present, it becomes colorimetrically labeled. The sample fluid carries the labeling agent down the test strip, whether or not antigen is present. The sample then encounters the test line

where antibodies against the target antigen are immobilized. If target antigen is present it becomes sandwiched at the test line between the immobilized antibody and the labeling agent concentrating the colorimetric indicator in an easily visualized line. The sample finally reaches the control line downstream from the test line where a secondary antibody against the labeling agent concentrates the labeling agent in a visually detectable line. Labeling agent is present in excess so when antigen is present there is still enough unbound labeling agent to form a control line. A positive result shows a line at the test line and at the control line whereas a negative result shows a line only at the control line.
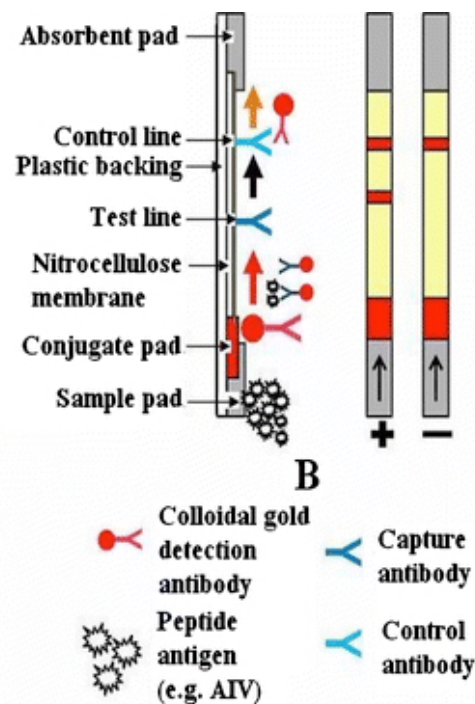
Figure 1. Lateral flow assay design. [1]

6

Most LFAs for malaria target *pfHRP2* in a sandwich assay format using monoclonal antibodies as the target recognition element. Colorimetrically labeled polystyrene beads, liposomes, and gold nanoparticles are common labeling agents. Gold nanoparticles form visible lines due to surface plasmon resonance shift when they become concentrated causing a color change from light red to dark blue.

Currently available RDTs do not meet the demands of point-of-care malaria testing. Antibodies are notoriously sensitive to storage and operating temperatures. Antibody-mediated tests therefore lack sufficient robustness and shelf life. RDT performance has been shown to be adequate in the hospital environment [19] but degraded in harsh conditions [20]. Moreover, reports have indicated mutations in *pfHRP2* can negatively affect test sensitivity depending on the region [21]. A second major problem with RDTs is parasitemia-dependent test sensitivity. A recent study has found overall RDT sensitivity of 92.6% for samples containing 500-1,000 parasites per µL [22]. However, 84% of malaria infections occur with parasitemia levels < 500 parasites per µL [23, 24]. RDT sensitivity falls to 89.3% and 53.9% for parasitemias of 100-500 and 0-100 parasites per µL, respectively. The WHO recommends a minimum 95% sensitivity for parasite densities of 100/µL [25]. Currently available RDTs do not exhibit adequate sensitivity for the most clinically meaningful parasitemia levels. Moreover, approximately 10.8 million RDTs were distributed to Africa in 2006 [26]. With an average unit price of USD$2-10, point-of-care testing is an economic burden to countries with the greatest incidence of malaria.

Assay Design

To address robustness, cost, ease-of-use, and performance problems with current RDTs for malaria detection, we propose an alternative antibody-free approach that enables intuitive noninstrumented signal visualization (Figure 3). The proposed assay is an aqueous solution containing two different colored polystyrene particles (red and green) and a magnetic particle (Figure 4). The green polystyrene particle and the magnetic particle are surface functionalized with nickel nitrilotriacetic acid (NiNTA), which serves as the antigen recognition element. NiNTA readily binds the histidine residues abundantly present in the *pfHRP2* molecule. A patient sample (saliva or serum) is mixed with the particle solution, and the *pfHRP2* cross-links a green particle to a magnetic particle. A drop of the mixed solution is then deposited on a substrate centered over a magnetic field and allowed to evaporate. The same unique capillary flow that causes rings to develop in an evaporating coffee drop – known as the "coffee stain phenomenon" – transports particles to the edge of the drop. As the sample dries, particles become concentrated on the edge resulting in a visually detectable colorimetric ring. In the case of an infected sample (i.e. *pfHRP2* is present), the green particle is cross-linked to a magnetic particle and thus immobilized at the center by the magnetic field. The red particle flows to the edge. On the other hand, an uninfected sample does not cross-link the green and magnetic particles so both green and red particles are transported to the edge. Therefore, a positive test results in a red ring and green center whereas a negative test results in a yellow ring (red + green) and a brown center (magnetic particle only). The assay combines the unique microfluidic behavior of an evaporating drop with a

simplified analog of the sandwich enzyme-linked immunosorbent assay (ELISA). Using the natural capillary action induced by the evaporative process eliminates the need for an onboard power source. Moreover, by relying on the recognized metal binding capacity of *pfHRP2* we circumvent the complexities and stringent storage and operating conditions necessary for optimal antibody function. The proposed assay consists of two steps: (a) mix the sample with the particle solution; (b) deposit a drop of mixed solution on the substrate to dry. The test result is then visually determined by the color of the dried residue. The proposed diagnostic design is easy to use, inexpensive to manufacture, stable over a variety of environmental conditions and duration, and easily interpreted by an unskilled user. A further advantage of the proposed assay over existing RDTs is the potential to be semi-quantitative. Both the size and color shade of the resulting ring are dependent on the number of *pfHRP2* molecules present in the patient sample. A greater number of *pfHRP2* molecules will cause more green particles to become immobilized. Red particles will then be present in greater proportion at the ring resulting in an orange appearance. Fewer *pfHRP2* molecules results in more free green particles and a ring having a yellow appearance. Ring size and color can enable quantification of *pfHRP2*, a known indicator of parasitemia, which holds clinical utility as more advanced infections can be triaged appropriately. It may be unrealistic for a layperson to accurately distinguish and interpret ring size and shade. However, a simple photograph could be evaluated either by a trained professional or by image processing software, for example an application on a smart phone. The same assay could potentially be used for both simple binary rural triage and more advanced quantification in the point-of-care setting and reference laboratories.

Coffee Stain Phenomenon

The proposed assay is based on the physics of an evaporating drop. When a drop of coffee is left to evaporate on a solid surface, the outcome is a dense ring of coffee particles at the perimeter of the drop. The underlying mechanism was first described by Deegan [2, 27]. When the drop is deposited ($t = 0$), particles are homogenously distributed throughout the solution. As solution evaporates, particles are transported by a radially-directed, surface tension-driven flow toward the edge of the drop. This flow proceeds until the end stage of the evaporation process at which point virtually all of the solute has been transported to the edge resulting in a dense annulus of particulate residue. Deegan determined three requisite conditions: (1) the solvent meets the surface at a non-zero contact angle, (2) the contact line is pinned to the substrate, and (3) the solvent evaporates. Mechanisms typically responsible for solute transport, for example simple diffusion, electrostatic interactions, surface tension gradients, and gravitational effects, are not responsible for the radial flow in an evaporating drop. In fact, these forces are more likely to disrupt ring formation instead of promote it. Rather, the microfluidic flow is the result of a geometric constraint imposed by a pinned contact line and differential evaporation rates between drop center and edge.

The evaporation rate is heterogeneous across the surface of the drop with a maximum occurring at the edges and minimum at the center [2]. During the evaporative process, solvent molecules rapidly interchange with the gas phase at the liquid-gas interface. The vapor then diffuses outward. The rate of this process depends on the difference in partial pressures between the solvent vapor and the ambient gas. Solvent vapor pressure reaches

equilibrium along the drop surface and diffuses into ambient conditions above the saturated surface.   At the drop edge, the solvent gas is bounded both above and to the side by ambient conditions thus providing evaporated gas a greater volume into which it can diffuse resulting in a higher evaporation rate compared to the drop center.

Surface tension effects dictate the shape of the spherical cap, which must remain relatively constant during the evaporation process. With solution leaving the drop at a greater rate at the edge and the contact line cannot recede to compensate for this loss of mass (and thus maintain drop shape), a current must flow from the center to the edge to replenish solvent lost to evaporation. This radial flow is transport particles or solute in solution to the edge during drop evaporation. Deegan et al [28] model the system as an axisymmetric drop (Figure 2).

Figure 2. Modeling flow in an evaporating drop. [2]
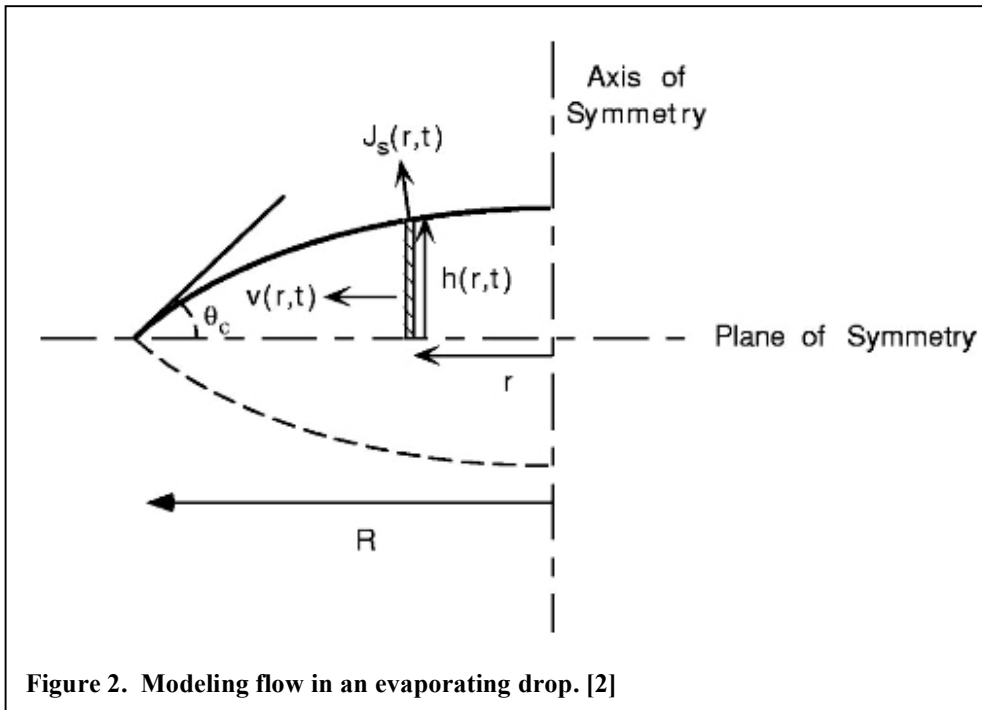
The rate of change in the amount of solution in an infinitesimally small annular element at distance r from the drop center equals the net flux of fluid flowing into the element less the mass of fluid lost to evaporation:

$$\rho\frac{\partial h}{\partial t} = -\rho\frac{1}{r}\frac{\partial}{\partial r}(rhv) - J_s(r,t)\sqrt{1+\left(\frac{\partial h}{\partial r}\right)^2} \qquad (1)$$

where ρ = density of liquid; r = distance from center; h = height; v = flux; $J_s(r,t)$; t = time

By solving for v, Deegan shows a nonzero v arises when there is a difference between the local evaporation rate and the net evaporation rate across the entire surface:

$$v(r,t) = -\frac{1}{\rho r h}\int_0^r r\left(J_s(r,t)\sqrt{1+\left(\frac{\partial h}{\partial r}\right)^2} + \rho\frac{\partial h}{\partial t}\right)dr \qquad (2)$$

To calculate flux, drop height and evaporation rates must be estimated. By assuming the drop profile approximates a spherical cap, height as a function of distance from center and time is derived from the Navier-Stokes equation:

$$h(r,t) = \sqrt{\left[\frac{h(0,t)^2 + R^2}{2h(0,t)}\right]^2 - r^2} - \frac{R^2 - h(0,t)^2}{2h(0,t)} \qquad (3)$$

The evaporation rate at the contact line is estimated as:

$$J_s(r,t) \sim (R-r)^{-\lambda} \qquad (4)$$

where $\lambda = (\pi - 2\theta_c)/(2\pi - 2\theta_c)$ and θ_c is the contact angle.

When a drop of particle-containing solution is deposited on a substrate, particles are homogenously distributed throughout the drop. The particles residing at the edge of the drop become trapped at the liquid-gas-substrate interface due to surface tension interactions during the early stages of evaporation. These particles protrude through the liquid-gas interface causing the contact angle to be greater than it would in the absence of particles. The local capillary force exerted between the substrate, liquid, and the protruding particle results in a pinned contact line if it exceeds the inwardly directed forces that result from the liquid-gas surface tension during evaporation. This criterion is satisfied as long as the decrease in contact angle due to evaporation is offset by an increase in contact angle caused by new protruding particles reaching the edge [29]. According to this criterion, contact line pinning is dependent on five variables: particle size, particle volume fraction, drop radius, evaporation rate, and the wetting characteristics of the substrate. Sangani et al [29] derived a mathematical criterion for contact line pinning based on empirical observations:

$$\Psi \equiv \varphi C_a \frac{R^4}{a^3 h_0} \geq C \equiv \frac{16}{9\lambda n_c} \qquad (5)$$

Where a = particle radius; R = drop radius; λ = drag coefficient; and φ = volume fraction (particles in solution). Equations (1) – (5) comprise a basic mathematical characterization of the mechanism that underlies the coffee stain phenomenon. These equations describe contact line pinning and radial flow dynamics. An additional relationship that affects ring structure development in a drying drop is the rate at which particles in solution fall to the substrate, known as settling or sedimentation velocity.

13

Stoke's law describes settling velocity as a function particle density, particle size, fluid density, and fluid viscosity:

$$V_s = \frac{2}{9}\frac{(\rho_p - \rho_f)}{\eta}gR^2 \qquad (6)$$

where V_s = settling velocity; ρ_p = particle density; ρ_f = fluid density; η = fluid viscosity; R = particle radius; and g = acceleration due to gravity

Large and sufficiently dense (relative to solution) particles settle at a faster rate relative to the radial velocity and sediment before reaching the edge. Less dense particles, for example polystyrene, accumulate almost completely at a drop edge.

Objectives

We seek to demonstrate that the same mechanism that causes rings to form in drying coffee drops can be used as a diagnostic assay potentially suitable for malaria detection in low-resource environments. This body of work represents a proof-of-principle encompassing the design of a three-particle assay, the characterization and optimization of basic design parameters, and capability assessment. The assay is designed to detect poly-l-histidine, a molecular mimic of *pfHRP2*.

CHAPTER II

**LOW-RESOURCE DIAGNOSTIC ASSAY BASED ON DISRUPTION OF
RADIAL FLOW IN AN EVAPORATING DROP**

Joshua R. Trantum[1]
Joshua D. Swartz[2]
David W. Wright[2]
Frederick R. Haselton[1,3]

[1]Department of Biomedical Engineering
Vanderbilt University
Nashville, Tennessee

[2]Department of Chemistry
Vanderbilt University
Nashville, Tennessee

[3]Department of Ophthalmology and Visual Sciences
Vanderbilt University Medical Center
Nashville, Tennessee

Corresponding Author:
Rick Haselton
Biomedical Engineering
Box 1510 Station B
Vanderbilt University
Nashville, TN 37235

615 322-6622
615 343-7919 FAX
rick.haselton@vanderbilt.edu

Introduction

Infectious diseases represent a major health and economic burden to many developing nations. The region most affected is Sub-Saharan Africa where infectious disease accounts for greater than 95% of all deaths [4]. Malaria is one of the most pernicious killers. In 2008, more than 250 million people worldwide were diagnosed with malaria and 881,000 succumbed to the disease [11]. In Sub-Saharan Africa, approximately 709,000 died of the disease in 2008 [5]. Malaria treatment accounted for 40% of total 2006 healthcare spending and represents a 1.3% drag on gross domestic product [4]. One culprit for these unfortunate statistics is the lack of pervasive early and accurate diagnostic testing [6].   Sub-Saharan Africa lacks a distributed infrastructure capable of high throughput advanced screening techniques. Reference laboratories exist in the urban centers, far removed from most afflicted patients. Patient samples often don't make it to the labs for testing, and the labs are mostly capacity constrained. Point-of-care (POC) testing is the most effective way of triaging symptomatic individuals. Point-of-care diagnostic devices must be low cost, simple-to-use, and non- or minimally instrumented to be effective in the rural setting. Moreover, the devices must be able to withstand harsh storage and operating conditions. Several products, known collectively as rapid diagnostic tests (RDTs), are currently available. These devices rely on immunochromatographic (i.e. lateral flow) techniques in which antibodies against the analyte are immobilized on nitrocellulose and interact with sample flowing via capillary (wicking) action. Captured analyte is concentrated in a discrete line, and signal is visually detected and interpreted. The analyte most often target for malaria testing is histidine rich protein, a protein secreted by the leading malaria-causing parasite species,

P. falcaparum. Currently available RDTs suffer two major shortcomings. The devices rely on antibodies as the analyte recognition element, and antibody function is notoriously sensitive to environmental conditions. Moreover, any genetic mutation in the HRP epitope region will impact antibody binding and test sensitivity.

We propose an alternative diagnostic assay design (Figure 3) that is robust, low cost, simple to use, and enables noninstrumented signal visualization. The design relies on the same phenomenon that causes a ring to form in a drying coffee drop. This previously characterized mechanism [2, 27-32] generates a radial capillary flow that concentrates the colorimetric indicator at the edge of an evaporated sample drop. Presence of HRP disrupts the radial flow of one colorimetric particle (Figure 4A). A secondary control colorimetric particle (Figure 4C) is transported to the edge whether or not HRP is present. Signal is visualized as a red ring in the positive case (red particle only at the edge) or as a yellow ring in the negative case (red+green particles at the edge). The assay uses nickel-nitrilotriacetic acid (NiNTA) as an alternative to antibodies for HRP recognition. Assay particles are surface modified with NTA, a metal chelator that coordinates nickel. Nickel has previously been shown to readily bind histidine residues, a technique commonly used for protein separation and purification with histidine tags [33]. The replacement of antibodies with NiNTA as the antigen recognition element results in an assay theoretically stable over long periods and harsh conditions.

In this work we demonstrate proof-of-principle using poly-l-histidine as an HRP biomolecular mimic. Basic design parameters are evaluated and optimized and system sensitivity and specificity are assessed.

17
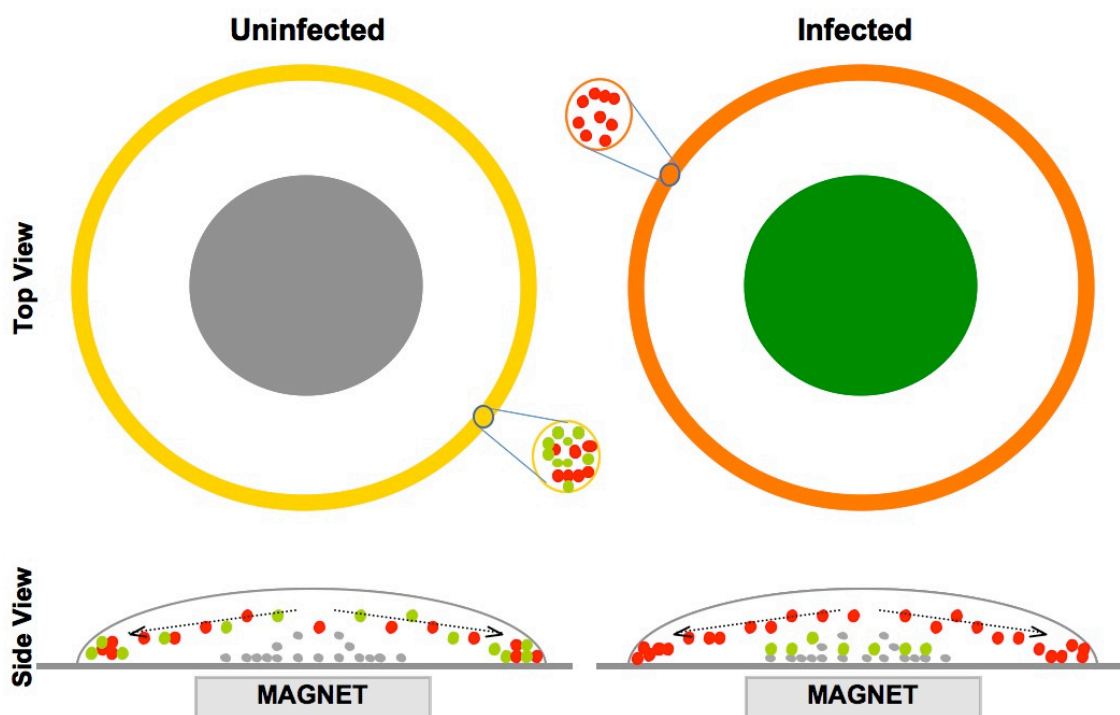
Figure 3. Schematic of two-color diagnostic assay. Left panel: an uninfected sample generates a yellow ring because the absence of HRP means the green particle is not cross linked to the iron oxide particle and is free to migrate to the edge. The co-location of both red and green particles at the edge results in a yellow ring. Right panel: HRP in an infected sample cross-links the green particle to the iron oxide, which is immobilized by the magnetic field at the drop center. Only red particles migrate to the edge resulting in a red ring and green center.
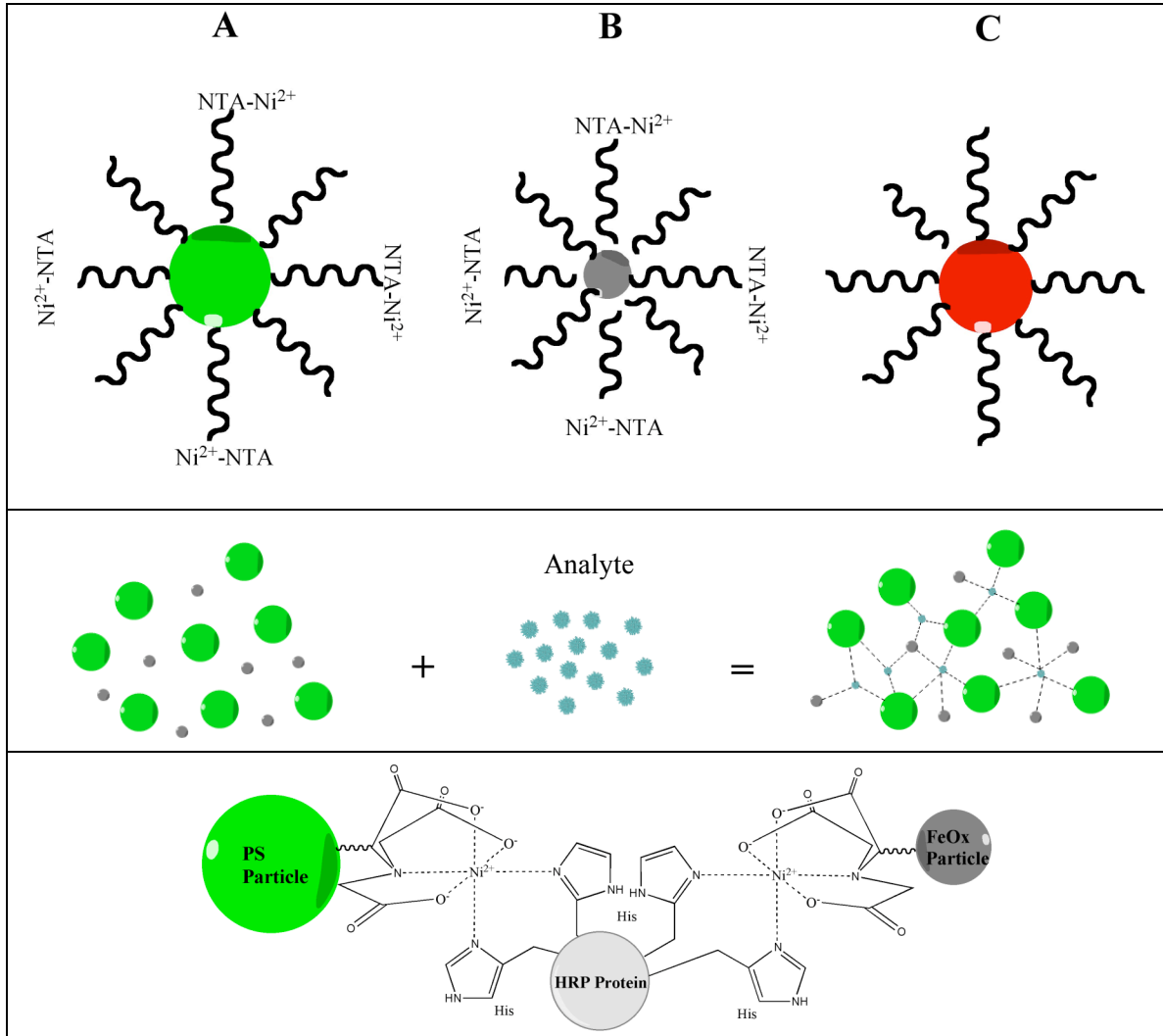
Figure 4. Surface chemistry and particle-particle interactions. Upper panel. The proposed assay consists of three particles: (A) 1µm diameter green fluorescent polystyrene; (B) 250nm diameter dextran-coated iron oxide; (C) 1µm diameter red fluorescent polystyrene. Particles (A) and (B) are surface modified with PEG groups terminated with Ni-NTA and a PEG backfill ligand. Particle (C) is pegylated. Center panel. When the two particles functionalized with NiNTA come in contact with analyte, histidine residues in the analyte cross-link the particles. Lower panel. Nitrilotriacetic acid (NTA) chelates Ni, which in turn coordinates with histidine residues in the HRP molecule.

Methods

Particle Functionalization

<u>PEGylation</u>

Polystyrene beads surface-modified with carboxylic acid groups and having a mean

diameter of 0.97μm were obtained from Bang's Laboratories with two different

fluorescence excitation/emission profiles: 540/600 (red, p/n FC03F/9803), and 480/520

(green, p/n FC03F/9927). The beads were washed by centrifugation three times (at 4.6g

for all wash steps) and re-suspended in 100mM PBS (pH 7.2) at stock concentration

$(1.975 \times 10^{10}$ per mL). The carboxylic acid groups were made sulfhydryl reactive by

reacting the particles with BMPH (Fisher Scientific, p/n 22297) in the presence of EDC

(Sigma Aldrich, p/n E7750). The BMPH was dissolved in PBS (pH 7.2) and added to the

particle suspension at a ten-fold molar ratio to carboxyl sites. EDC dissolved in 100mM

MES buffer (pH 4.9) was immediately added to the reaction volume to yield a fifty-fold

molar excess relative to carboxyl sites. The reaction volume incubated at least two hours.

Particle suspensions were then washed three times via centrifugation and re-suspended in

PBS (pH 7.2). The red control particles were pegylated by reacting with thiol-PEG-

methyl (Quanta Biodesign Ltd, p/n 10793) dissolved in PBS (pH 7.2) to yield a ten-fold

molar excess relative to maleimide groups. The suspension incubated for at least two

hours, was washed three times via centrifugation, and re-suspended in deionized water.

The green particle suspension was reacted with a solution containing both thiol-PEG-

methyl (backfill ligand) and thiol-PEG-carboxylic acid (Quanta Biodesign Ltd, p/n 10793

and 10183, respectively) dissolved in PBS (pH 7.2), the ratio of which ultimately

determines NiNTA surface coverage (10%, 30%, 50%, and 80%). The suspension

incubated for two hours, was washed three times via centrifugation, and was re-suspended in MES buffer (pH 4.9).

Conjugation of NTA to polystyrene particles

EDC and sulfo-NHS (Sigma Aldrich, p/n 56485) were together dissolved in MES buffer (pH 4.9) at a molar ratio of 1:2.5. The EDC/NHS solution was added to the reaction volume (in MES) such that there was a ten-fold molar excess of EDC to carboxyl sites. The solution reacted for fifteen minutes at room temperature, washed three times via centrifugation, and re-suspended in PBS (pH 7.4). A solution of nitrilotriacetic acid (Sigma Aldrich, p/n 14580) in PBS (pH 7.2) was added to yield a ten-fold molar excess relative to active sites. The reaction volume reacted for two hours, washed via centrifugation, and re-suspended in 100mM HEPES buffer (pH 7.2).

Coordinating nickel to polystyrene-PEG-NTA particles

Nickel chloride is dissolved in deionized water and added to PEG-NTA-conjugated particles (in HEPES buffer) to yield a ten-fold nickel molar excess over NTA groups. The reaction volume reacted two hours, was washed five times via centrifugation, and re-suspended in deionized water.

Coordinating nickel to iron oxide-NTA particles

Dextran-stabilized iron oxide particles having a mean diameter of 250nm and surface-modified with NTA were obtained from Micromod Gmbh (p/n 09-11-252). The particles were washed three times via magnetic separation (or centrifugation) and re-suspended in deionized water (0.2% Tween 20) at stock concentration (4.9×10^{11} per mL). Nickel chloride was dissolved in deionized water and added to the iron oxide-NTA particles to yield a ten-fold nickel molar excess over NTA groups. The reaction volume reacted for

two hours, was washed five times via centrifugation, and re-suspended in deionized water. The reaction volume reacted for two hours, was washed five times via centrifugation, and re-suspended in deionized water.

Particle Characterization

Particle concentration and size distributions of polystyrene particles were measured using a Beckman Coulter Multisizer 3 coulter counter. One microliter of stock particles was diluted in 20mL of Isoton II diluent (Beckman Coulter) and measured using a 30μm aperture. Iron oxide particle size distribution was measured using dynamic light scattering (Malvern Zetasizer) by diluting 20μL of stock particle solution in 1mL deionized water. Polystyrene and iron oxide particle surface modification was verified by measuring zeta potentials (Malvern Zetasizer) of the functionalized particles versus non-functionalized. For all zeta potential measurements, 20μL of particles were diluted in 1mL of 10mM PBS. For some batches, zeta potential was measured at intermediate steps to confirm a change in zeta potential with the addition of each functional group.

Particle count requirement for ring visualization

The proposed assay must contain enough fluorescent particles so that a ring can be visually detectable when the particles are concentrated at the edge of the drop. To determine the minimum number of particles required, 0.97μm diameter carboxylated polystyrene particles (Bang's Labs) were serially diluted in deionized water (10^7, 10^6, 10^5, 10^4, and 10^3 per μL), deposited in 3μL drops in triplicate on a plain glass slide, allowed to evaporate, and imaged using a Nikon TE2000U inverted fluorescence

microscope. The process of perceiving a ring shape within an image incorporates not only objective physical aspects of the imaged object, but also subjective variables such as visual acuity and psychology. The subjective components are beyond the scope of this work. However, in order to more precisely evaluate perceived ring formation, a Matlab simulation was created and used to model rings composed of different particle counts (Appendix B). This data was used to corroborate the results from the serial dilution experiment.

Order of addition experiment

The order in which each of the three particles interacts with PLH is likely to have an impact on assay sensitivity due to competition for binding sites. To determine the order of particle addition that generates the greatest amount of green-iron oxide co-location, three different orders were considered: (1) PS-PEG-NiNTA + PLH (sixty minutes), then add iron oxide-NiNTA (thirty minutes); (2) Iron oxide-NiNTA + PLH (thirty minutes), then add PS-PEG-NiNTA (sixty minutes); and (3) PS-PEG-NiNTA + Iron oxide-NiNTA, then add PLH (ninety minutes). The red control particle was excluded from the experiment to isolate the variable of interest, binding site competition. PLH was obtained from Sigma Aldrich (p/n P9386). The concentration of PLH used in all three samples was 1.74μM in deionized water. The starting concentrations of PS-PEG-NiNTA and iron oxide-NiNTA were $2x10^7$ per μL and $4x10^7$μL, respectively. Each reagent was added in equal volumes (5μL). Three microliter drops were manually pipetted onto a plain glass slide in triplicate using the magnet-slide apparatus (Figure 5). The plain glass slide was rinsed with deionized water and dried with a Kimwipe immediately prior to use. Once

the drops dried the slide was removed from the apparatus and imaged using a Nikon

TE2000U inverted fluorescence microscope.
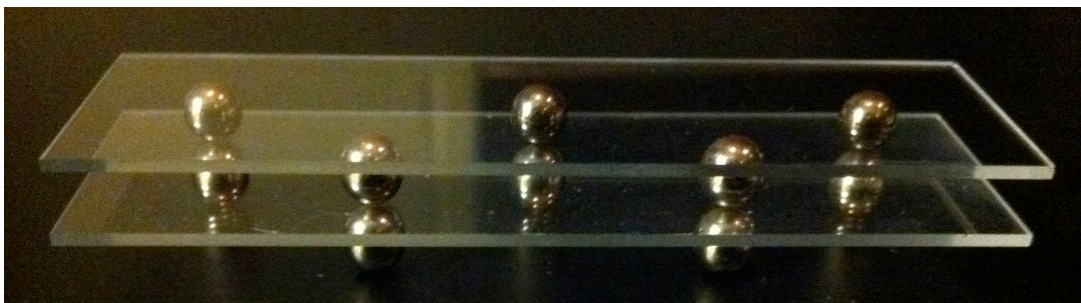
Figure 5. Magnet-slide evaporation apparatus. The base of the device is a regular glass slide sandwiched between two spherical magnets at five different points. A second glass slide (substrate) is placed on top of the magnet pairs. Sample drops are manually deposited on the substrate centered above each magnet. Sandwiching the base slide between magnet pairs ensures magnetic poles are aligned normal to the substrate.

Determination of optimal Ni-NTA surface coverage

The number of Ni-NTA sites per green polystyrene particle is expected to affect assay

performance because the greater this number, the more PLH molecules are required to

shift a green particle to the center. In other words, the greater number of cumulative

NiNTA sites in the assay, the greater the PLH count the system can absorb before

generating signal. The number of NiNTA sites per polystyrene particle is dictated by

controlling the ratio of thiol-PEG-methyl (backfill ligand) to thiol-PEG-carboxyl during

particle surface functionalization. To determine the most appropriate NiNTA surface

coverage ratio, four different batches of PS-PEG-NiNTA were fabricated each with a

different coverage ratio (% NiNTA): 10%, 30%, 50%, and 80%. A two-particle assay

was performed using the same methodology as that used in the order of addition

experiment. Images were analyzed using Image Pro Plus software (version 7.0). Four

areas-of-interest (Figure 6) were defined *a priori* and fluorescence intensity was

measured for each. The same areas-of-interest were used for each image. Due to

position variability during manual drop deposition the location of settled magnetic

particles relative to the ring varies from drop to drop. Areas of interest in the software

program were manually moved to the appropriate location in the image prior to taking the

measurement. Total and mean intensities (green channel only) were recorded. The area

of each region was calculated as the ratio of the two intensities. Mean background noise

multiplied by each AOI area was subtracted from each respective AOI total intensity

value. Signal to noise was then calculated using intensity values corrected for

background as: A / (B − A) (Figure 6).

Determination of optimal particle concentrations

The ratio of PS-PEG-NiNTA : Iron oxide-NiNTA : PLH is expected to be a critical

relationship due to competitive binding characteristics and the total number of NiNTA

sites relative to the number of PLH molecules. The ratios of these three components

were evaluated using the same methodology used in the determination of optimal NiNTA

surface coverage experiment. Using a 384-well plate, a matrix of varying [PS-PEG-

NiNTA] and [iron oxide-NiNTA] was generated. Iron oxide-NiNTA initial

concentrations (per μL) evaluated were: $4x10^7$, $3x10^7$, $2x10^7$, $1x10^7$. PS-PEG-NiNTA
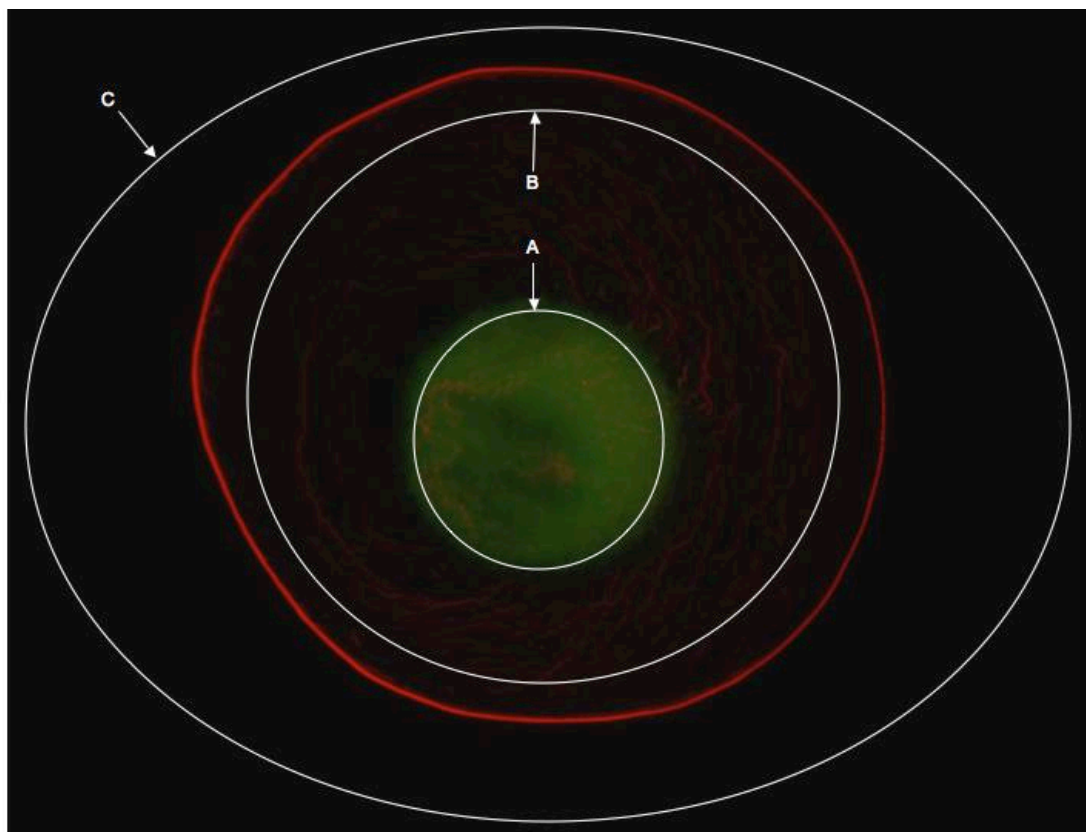
Figure 6. Areas of interest for intensity measurements. (A) area of interest is placed around the magnetic particles that accumulate in the drop center above the magnetic field lines. In a positive sample, green particles co-locate with magnetic particles – the fluorescence intensity of which represents signal in the system. (B) secondary inner area of interest captures both signal in the center and particles that have non-specifically and randomly settled throughout the inner region. (C) outer area of interest measures the total fluorescence intensity of the drop. (B) – (A) represents noise. (A) represents signal. (C) – (B) represents a surrogate marker for both signal and noise since particles not transported to the edge either non-specifically settle in the inner region as noise or specifically trans-locate to the center as signal.

initial concentrations (per µL) evaluated were: 1.3×10^7, 1×10^7, 7×10^6, 3.86×10^6. The

particles were pre-mixed in each well and then 435nM PLH was added and incubated for

thirty minutes. Three microliter drops were deposited on a plain glass slide in triplicate

on the magnet-slide apparatus. Fluorescence intensities were measured for each image

and signal-to-noise was calculated. The three SNR calculations were averaged for each data point and the mean plotted.

Assay limit of detection

To assess assay performance, a three-particle assay was performed at varying concentrations of PLH: 1.74μM, 870nM, 435nM, 218nM, 109nM, 0nM. At each concentration a control assay was performed using poly-l-aspartic acid in place of poly-l-histidine. PLAA was obtained from MP Biomedicals, LLC (Fisher Scientific, p/n 151909/lot#4716K) and dissolved in deionized water. Five microliters of PS-PEG-NiNTA ($3.86x10^6$ per μL) particles were mixed with five microliters of iron oxide-NiNTA ($1x10^7$ per μL). PLH or PLAA was added to the particle solution and allowed to incubate for thirty minutes. Five microliters of the red control particle, PS-mPEG ($3.86x10^6$ per μL) was added to the reaction volume. Drops were then deposited in triplicate on a plain glass slide on the magnet-slide apparatus. In addition to the previously described signal-to-noise calculation, a surrogate signal calculation was made by calculating the green fluorescence intensity in the ring as a percentage of total ring fluorescence intensity (green + red). The ring is defined as AOI C-B (Figure 6). The three calculations are averaged per data point. The experiment was repeated two more times for an n=3. SNR values from the three experiments were averaged together and plotted.

Results

We determined the number of 1μm fluorescent polystyrene particles required to detect

a ring in a 3μL drop to be in the range of 10^5 to 10^7 per μL (Figure 7). A ring can be

detected with as few as $100 - 1{,}000$ particles per μL, but the ring structure is not wide

enough to be easily detected on a consistent basis. This is more clearly demonstrated in a

simulation of ring formation (Appendix B). The lower limit is dictated both by the

human eye's ability to resolve a thin ring structure and the minimum particle volume

fraction required to pin the contact line. The upper limit is bounded by the fact that a

certain percentage of particles in an evaporating drop will settle before reaching the

contact line. As the number of particles increases, a greater absolute number of particles

settle in the center making it more difficult to resolve a ring at the edge. In other words,

more non-specifically settled particles obscures the distinction between a clear ring and a

film of particles. Based on this study, in addition to the simulation, we determined that

the concentration of an indicator particle (red or green) in the final reaction volume must

fall within 10^5 to 10^7 per μL in order to generate an easily detectable ring. Assay design

used in variable analysis / optimization experiments were performed using polystyrene

concentrations within this range.
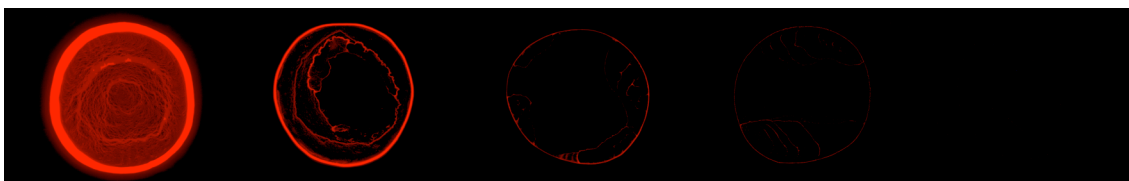
Figure 7. From left to right: the number of 1μm carboxylated polystyrene particles per μL in 3μL drops is progressively decreased: 10^7, 10^6, 10^5, 10^4, 10^3. A faint ring is detectable at 10^4.

The number of antigen recognition sites (NiNTA) per polystyrene particle affected assay performance both in terms of visual appearance (Figure 8) and signal-to-noise (Figure 9). Using a constant PLH concentration of 1.74μM, the 10% NiNTA coverage exhibited the greatest amount of green particle shift from edge to center followed by 80%, 50%, and 30% NiNTA coverage samples. This result is not consistent with the expectation that there would be a stepwise decrease in particle shift from edge to center as the percent NiNTA coverage increases. It is not evident to what degree the resulting particle shift in each sample represents specific versus non-specific binding to magnetic particles and/or substrate in the center. To be consistent, fluorescence intensity was measured using the same areas-of-interest for each image. In the case of the 10% NiNTA coverage sample, much of the center green particle mass lies outside the area of interest and is thereby classified as noise in the signal-to-noise calculation. SNR was maximized at the 50% NiNTA surface coverage level (Figure 9). As a result, green polystyrene particles used in subsequent experiments (order of addition, particle concentration, and limit of detection) were fabricated with 50% NiNTA surface coverage.
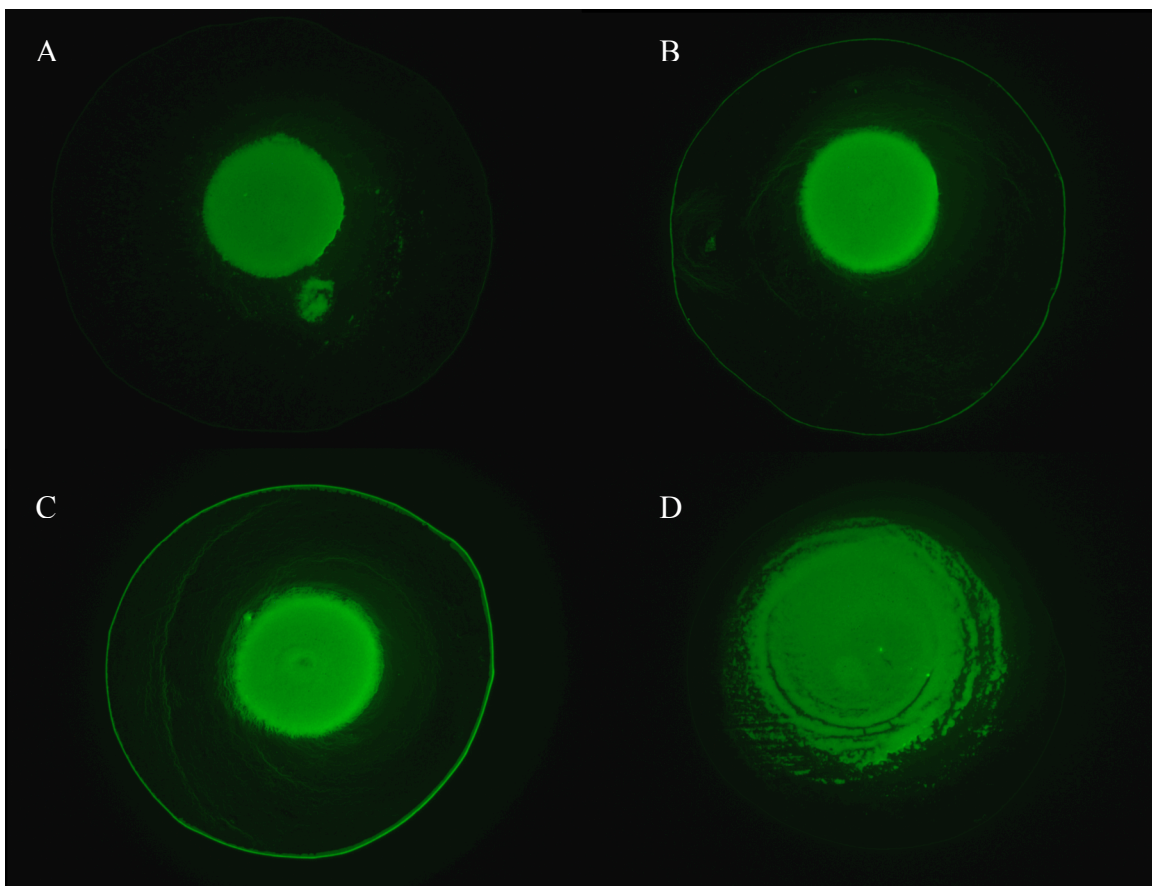
Figure 8. Varying NiNTA surface coverage on the polystyrene particle affects ring formation and particle distribution in a two-particle assay. (A) 80% coverage; (B) 50% coverage; (C) 30% coverage; (D) 10% coverage
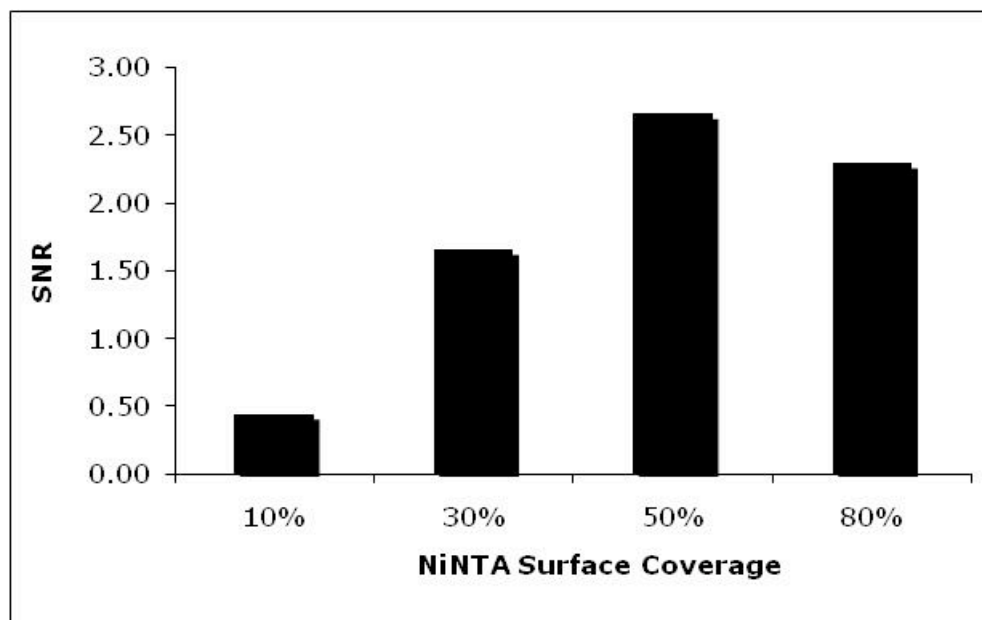
Figure 9. Signal-to-noise ratios generated in a two-particle assay with varying amount of NiNTA per polystyrene particle.

Optimal particle concentrations of PS-PEG-NiNTA to iron oxide-NiNTA were determined by varying each and calculating and comparing SNR at each combination. PLH concentration was held constant at 435nM. A peak signal-to-noise was found to coincide with polystyrene and iron oxide concentrations of 3.86×10^6 and 1×10^7 per μL, respectively (Figure 10). At this point the average SNR was 1.75 (n=3). These particle concentrations were used in subsequent experiments (order of addition, limit of detection).
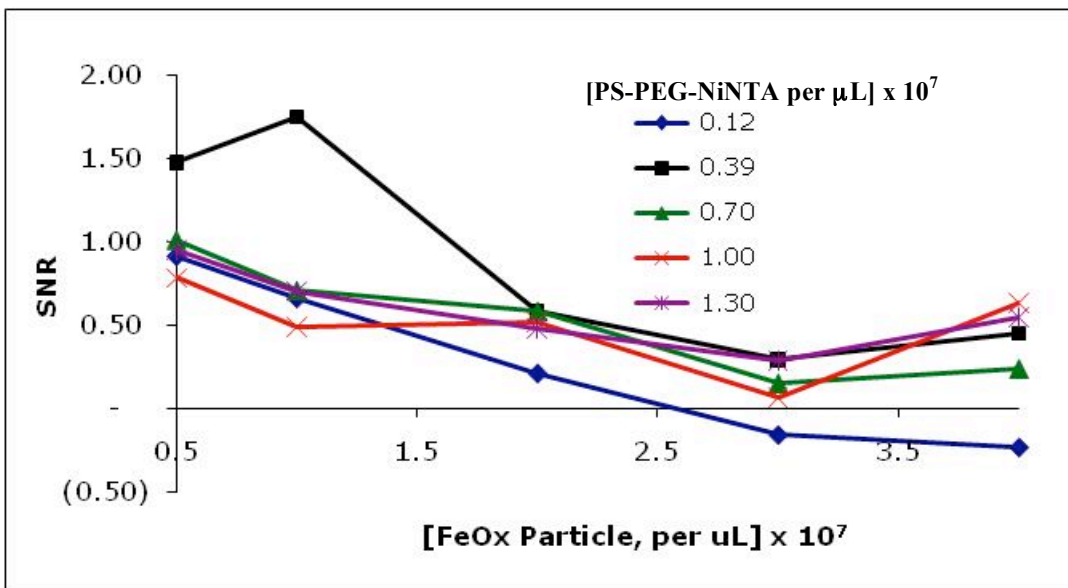
Figure 10. Signal-to-noise ratio generated in a two-particle assay with varying concentrations of polystyrene and iron oxide particles (n=3). Poly-l-histidine concentration was held constant at 435nM.

The results shown in Figure 11 indicate that pre-mixing the green polystyrene and iron oxide particles results in the best signal generation at low PLH concentrations. Due to competitive binding effects, the order of particle addition to a solution containing poly-l-histidine is expected to yield different signal-to-noise characteristics. To test this assumption and determine the optimal order of addition, we evaluated three different schemes at two different PLH concentrations (Figure 11): 1.74μM and 435nM. The optimal order of addition generates strong signal at both PLH concentrations. Signal here is defined qualitatively as green particles co-located with magnetic particles in the center of the drop. The order of addition resulting in the strongest signals at both low and high PLH concentrations is when the two particles are pre-mixed and then introduced to the PLH solution. Allowing iron oxide particles to incubate with PLH prior to adding polystyrene particles resulted in slight signal at 435nM PLH and broad signal at 1.74μM;

whereas incubating polystyrene with PLH first resulted in virtually no signal at low PLH concentrations and strong tightly packed signal at high PLH concentration. This difference can be explained by the difference in particle size. Since the iron oxide particles are 250nm diameter versus 0.97μm for the polystyrene, allowing the iron oxide to react with PLH first sterically hinders polystyrene from many available binding sites. But since the iron oxide is smaller, the polystyrene can still access some binding sites. When polystyrene is reacted with low PLH concentration first, the larger polystyrene sterically hinders the iron oxide from accessing nearly all available PLH binding sites. A similar particle size effect likely explains the difference in particle distributions at high PLH concentration. When polystyrene particles react with PLH first, the particles are cross-linked and saturated with PLH leaving abundant peripheral binding sites for iron oxide particles. Since the iron oxides are on the periphery, attraction to the magnetic field causes the entire particle mass to contract resulting in a tight pellet. Conversely, when iron oxide particles react first, subsequent polystyrene binding occurs mostly at the periphery so attraction to the magnetic field does not cause pellet contraction, but rather a broad distributed pellet. Based on these results, the scheme in which the green polystyrene and iron oxide particles are pre-mixed was used for subsequent experiments (limit of detection).
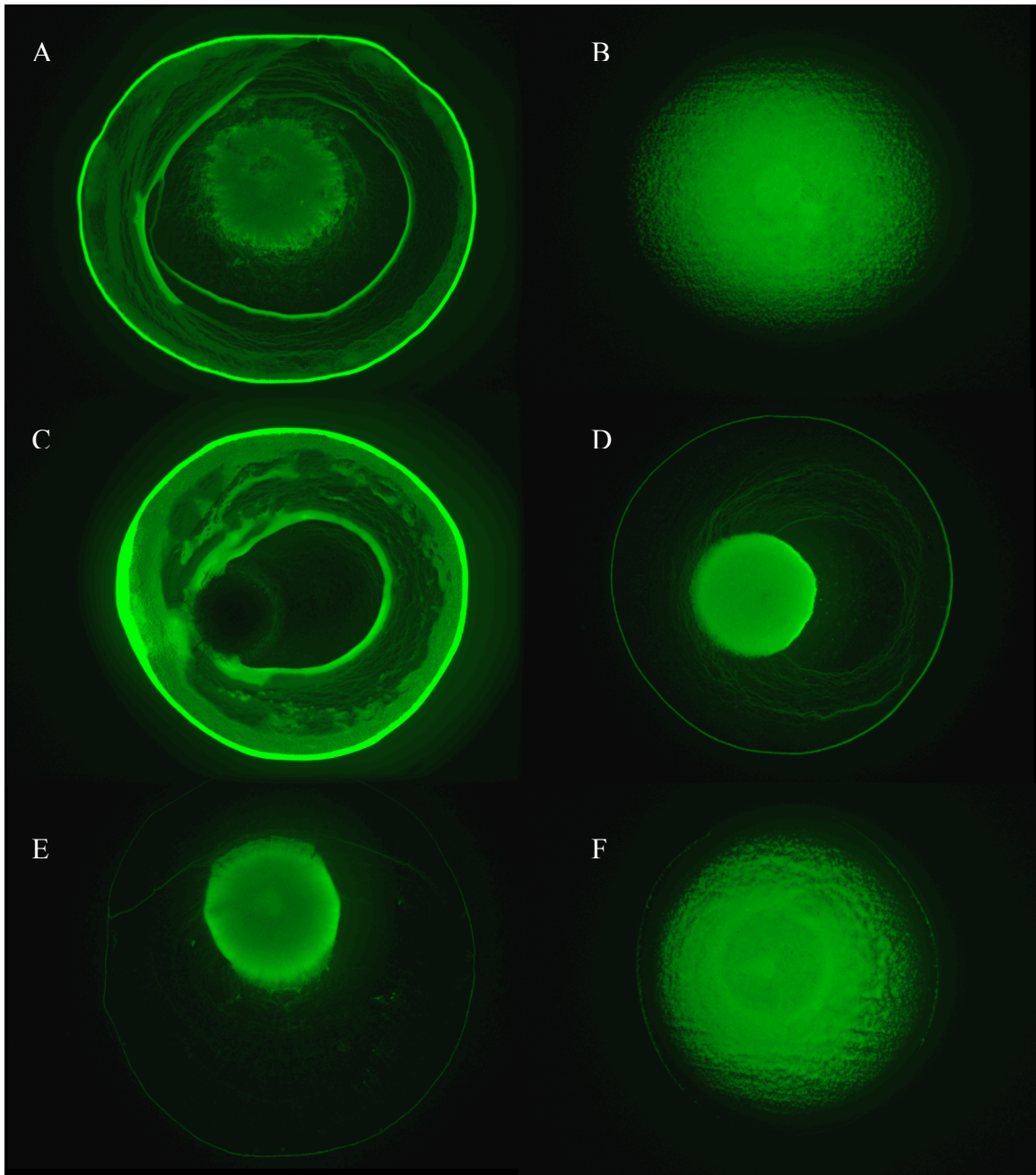
Figure 11. Order of addition affects particle distribution. Two-particle assays were performed at two different concentrations of poly-l-histidine (PLH), 435nM (left column) and 1.74μM (right column). (A) and (B): Iron oxide particles are incubated with PLH first then polystyrene particles are added; (C) and (D): Polystyrene particles are incubated with PLH first then iron oxide particles are added; (E) and (F): Polystyrene and iron oxide particles are pre-mixed and then PLH is added.

	Fluorescence	Phase Contrast
Positive		
Negative		
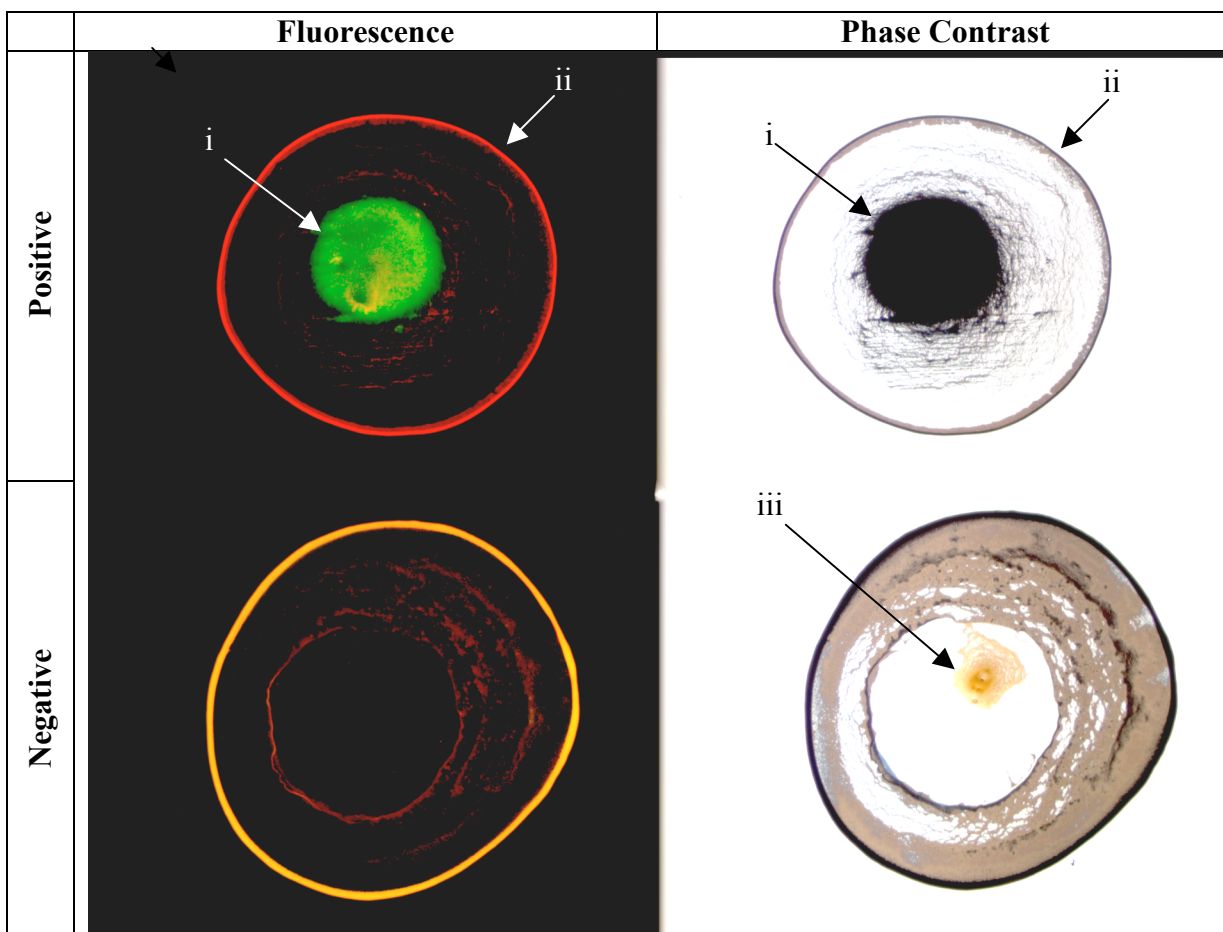
Figure 12. Three-particle assay at 1.74μM poly-l-histidine (top two rows) or 1.74μM poly-l-aspartic acid (bottom row, control). The right column is a phase contrast image corresponding to the fluorescence images in the left column. (i) Green particles are cross-linked to magnetic particles and immobilized in the center; (ii) red particles are free to migrate to the edge; (iii) magnetic particles in the center of the negative sample form a smaller area than in the positive sample because green particles are not cross-linked.

A three-particle assay in which the control particle (red PS-PEG) is added after target incubation was performed with varying levels of PLH using the optimized parameters determined in prior experiments. At each [PLH] a negative control assay was performed using an equivalent concentration of poly-l-aspartic acid. At the highest target concentration of 1.74μM the resulting fluorescence and phase contrast images

demonstrate a clear qualitative distinction between positive and negative (Figure 12). In the positive, the ring appears red while nearly all the green particles shifted to the center. Conversely, the negative images show a yellow/orange ring due to co-location of green and red particles. Further evidence that the negative ring is comprised of both polystyrene particles is demonstrated by the fact that the center pellet consists of only magnetic particles, which appear smaller and brown in color in the negative phase contrast image versus the positive. Representative images of both positive and negative (i.e. PLH or PLAA) assays at each target concentration level are shown in Figure 13 and demonstrate target concentration-dependent signal generation. Signal-to-noise (Figure 14) and the percentage of ring fluorescence due to green particles (Figure 15) quantitatively substantiate these observations.
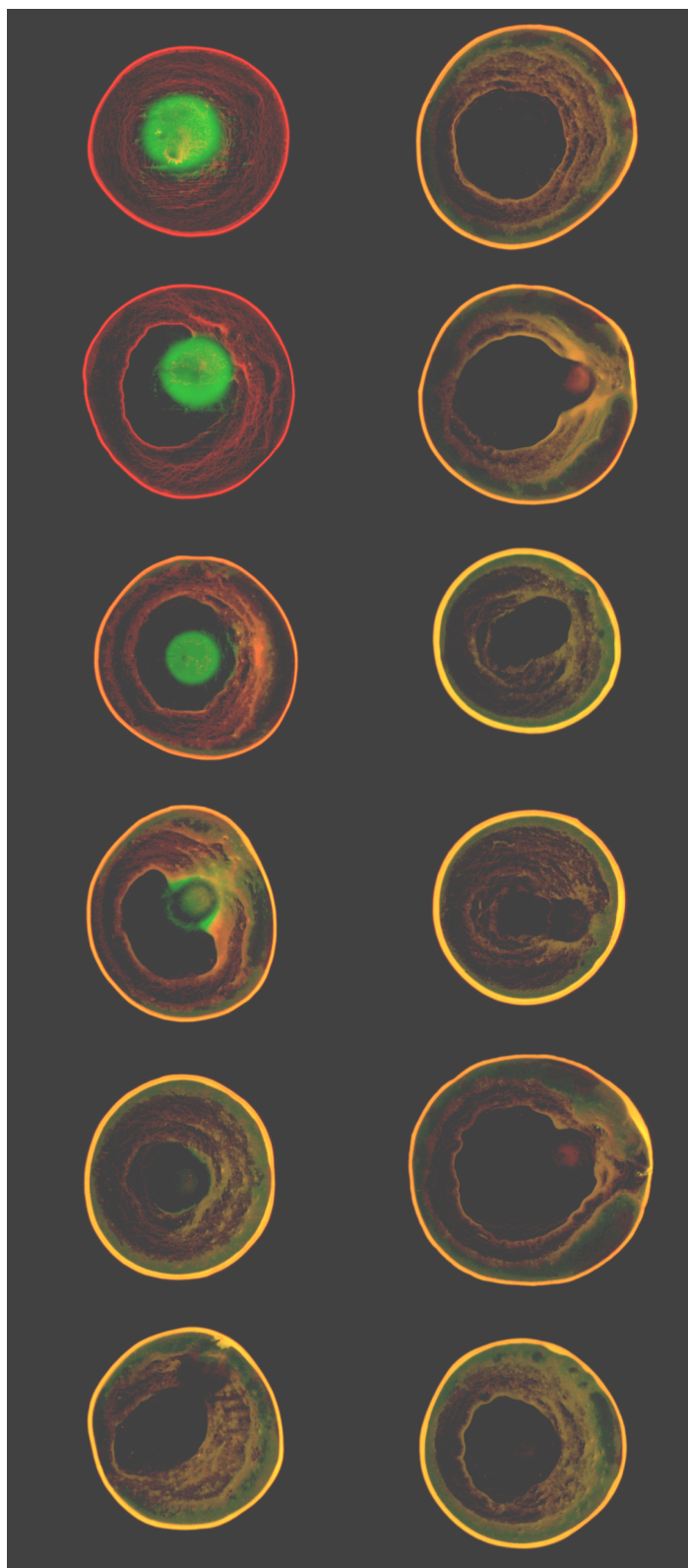
Figure 13. Concentration dependent signal generation in a three-particle assay. Poly-l-histidine (left column) and poly-l-aspartic acid (right column) concentration decreases down the rows: 1.74μM, 870nM, 435nM, 218nM, 109nM, 0nM. Signal, defined as a green center and a ring color shift from red to orange/yellow, decreases with decreasing poly-l-histidine concentration.
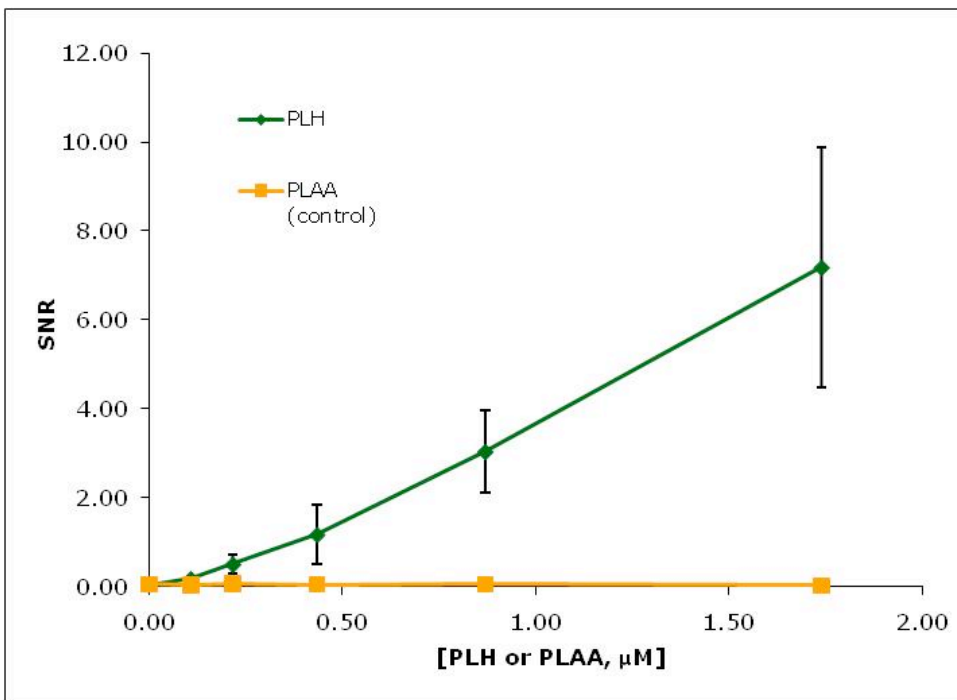
Figure 14. Limit of detection of the three-particle assay. Signal is measured as green fluorescence intensity in the center of the drop and noise is calculated as the green fluorescence intensity difference between the two inner areas of interest. Signal-to-noise ratio is plotted against [PLH] (positive) and [PLAA] (negative). SNR was calculated for three different drops at each [PLH or PLAA] per trial. Three trials were performed and the mean is plotted above. Error bars represent +/- one standard deviation (smaller than symbol in PLAA series).
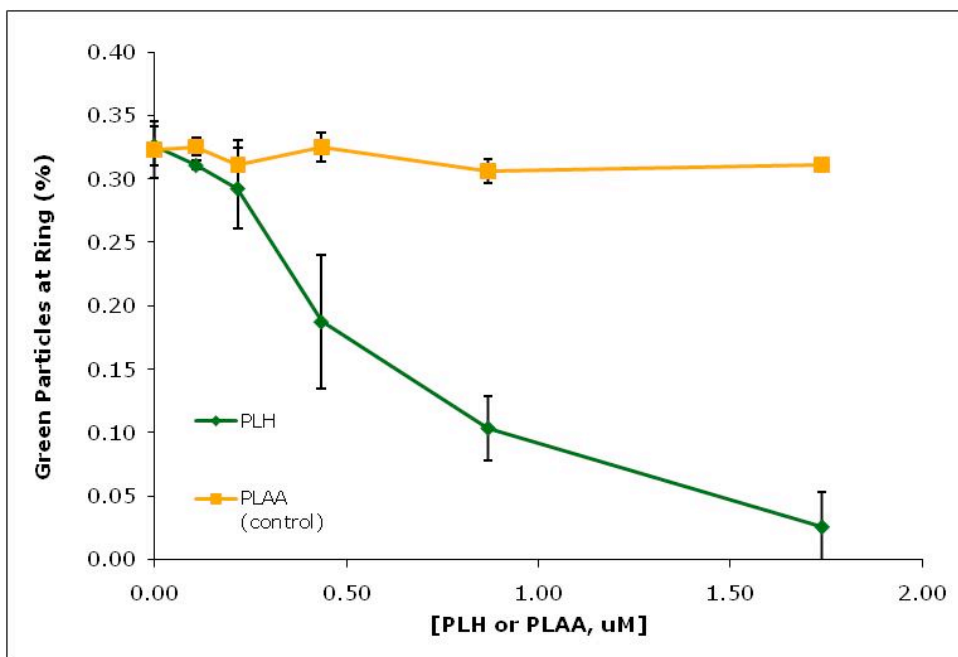
Figure 15. Limit of detection of the three-particle assay. Green fluorescence intensity as a percentage of green + red fluorescence intensity at the ring is plotted against [PLH or PLAA] as an alternative assay performance metric to signal-to-noise.

Discussion

The proposed three-particle assay generated distinctly different color patterns for samples containing poly-l-histidine versus samples with poly-l-aspartic acid (Figure 13). As PLH concentration decreases, the ring color becomes progressively more orange/yellow in color. Additionally, the region of green particles in the center becomes smaller and less noticeable. By contrast, the color patterns of all negative samples maintain a constant orange/yellow ring appearance with no green particle mass in the drop center. At low PLH concentrations, the positive becomes indistinguishable from the negative. This concentration-dependent image appearance suggests the assay correctly

identifies a solution containing PLH in a manner consistent with our expectations. Moreover, negative results generated at all concentrations of PLAA suggest the PS-PEG-NiNTA particles bind poly-l-histidine with specificity.

Both methods of quantifying the difference between positive and negative image appearance, presented in Figure 14 and Figure 15, confirm green particles shift from the ring to the center in a PLH concentration-dependent fashion. Signal to noise ratio (Figure 14) is a direct measure of green particle distribution. The numerator represents the green particles co-located with magnetic particles in the drop center and the denominator reflects green particles that have non-specifically settled in the drop center. An underlying assumption in this calculation is that all green fluorescence co-located with magnetic particles is due to PLH-mediated cross-linking between PS-PEG-NiNTA and iron oxide particles. One data point at the highest PLH concentration was excluded from the mean calculation due to a misaligned magnetic field.

The metric plotted in Figure 15 is an indicator of green particles shifted away from the ring that could be due to non-specific settling (noise) or PLH-mediated cross-linking to iron oxide. The metric represents the percent of ring fluorescence attributed to green particles. As expected, this value decreases with increasing poly-l-histidine concentration. Because the negative control remains fairly constant, the change in value for positive tests is most likely due to PLH-mediated cross-linking rather than non-specific settling. The PLAA values are fairly constant at approximately 0.33. Ideally the absence of PLH would be .50, meaning the ring consists of 50% green particles and 50% red particles. The actual value of 0.33 is likely due to a difference in fluorophore

brightness between the two polystyrene particles and/or error in particle concentration measurements.

The data presented in Figure 13, Figure 14, and Figure 15 suggest a limit of detection in the 200-500nM range. The gold standard methods of diagnosing malaria, thick film or thin smear microscopy or ELISA, test for the degree of parasitemia, that is the number of parasites present in a blood sample. These tests have a limit of detection < 20 parasites per µL whole blood [15-17]. Currently available RDTs detect surrogate markers of parasitemia like *pfHRP2*. There is currently a lack of consensus regarding the relationship between serum *pfHRP2* levels and parasitemia. However, recent research has determined currently available RDTs limits of detection to be ~ 100 parasites per µL, corresponding to approximately 800pM to 20nM *pfHRP* [19]. Based on this estimate and assuming poly-l-histidine suitably mimics *pfHRP2* nickel binding behavior, the proposed assay limit of detection is approximately one order of magnitude above the clinically relevant *pfHRP2* concentration. Several assay design parameters can be adjusted and optimized that would be expected to lower the limit of detection. The assay methodology employed relied on manual sample alignment and deposition and over a magnetic field. By incorporating a form-factor design that eliminates variability inherent in manual operation, signal-to-noise variability should decrease enabling statistical distinction between positive and negative samples at lower target concentrations.

Signal increases in the system – whether measured by ring color or center color – when a green particle is cross-linked to a magnetic particle and pulled to the center by the magnetic field. Assay sensitivity is therefore dependent on variables that affect how many target molecules (e.g. PLH) are required to cross-link green and iron oxide

particles. Theoretically, a single target molecule having more than one binding site can cross-link the two particles. However, since each particle has multiple NiNTA functional groups, they can bind many target molecules. By limiting the number of NiNTA functional groups on particle surfaces, this one-to-many relationship can be reduced thereby increasing sensitivity. In other words, a greater percentage of target molecules in solution serve the purpose of linking a green particle to a magnetic particle rather than saturating NiNTA groups on particle surfaces.

Signal generation is discretized, that is signal increases or decreases by the marginal impact of a single particle shifting from ring to center. By increasing particle size the signal that is produced by shifting one particle to the center increases. Signal detection relies on the operator's ability to visualize the ring. The total number of particles required to form a visually detectable ring is less when the particle size is larger. However, the upper limit on particle size is bounded by contact line pinning constraints (Equation 5, [29]). Previous studies have estimated this size to be approximately 10μm [29]. Incorporating both a larger green particle and limited number of NiNTA groups per particle, sensitivity of the assay is expected to increase by at least one order of magnitude.

Holding other variables constant, increasing particle concentrations reduces assay sensitivity. If for a given PLH concentration the concentration of green particles is optimized, then all green particles will be shifted to the center and none will transport to the drop edge. If the number of green particles increases at the same PLH concentration, there will not be enough target available to cross-link the extra particles to iron oxide particles and they will migrate to the edge adding more green to the ring. If on the other

hand the number of green particles is decreased, then signal will not be maximized because there will be PLH molecules present not being used to cross-link particles. Particle concentrations used to evaluate assay limit of detection (Figure 13) were determined by maximizing signal-to-noise at a poly-l-histidine concentration of 435nM (Figure 10). A multivariate regression model (Appendix F) was performed using [PS-PEG-NiNTA and [iron oxide-NiNTA] as independent variables and signal-to-noise as the dependent variable. The PS-PEG-NiNTA concentration was found to have a statistically significant positive effect on signal-to-noise (p-value < .001; t-statistic 3.55) within the concentration ranges studied. The iron oxide concentration did not have a statistically significant impact on signal-to-noise probably because the number of nickel binding sites on iron oxide particles exceeded those required at a [PLH] = 435nM. A lower limit of detection is expected using particle concentrations determined by optimizing signal-to-noise at a lower PLH concentration.

Particle composition and surface chemistry are both expected to impact assay limit of detection. Particle density affects settling velocity and ring structure. Dense particles with a settling velocity sufficiently higher than radial velocity results in more particles distributed throughout the center of the drop upon full evaporation. Moreover, any non-specific binding among dense particles magnifies the amount of particles likely to settle in the drop center. Antigen-induced agglomeration among dense particles will especially cause particles to fall out of solution before reaching the ring. This effect could be exploited to eliminate the need for a magnet in future designs.

Since surface chemistry modification reactions occur with sub-100% efficiency, particle composition wields an effect on particle-particle interactions. The classical

Derjaguin-Landau-Verwey-Overbeek (DLVO) theory describes the forces that affect colloid stability [34] and predicts that van der Waals and electrostatic forces dominate particle-particle interactions at the nanoscale. The correct balance of forces is necessary to maintain a stable colloidal solution. The presence of charged chemical species at the particle-liquid interface dictates solubility and interactions with other particles. The green polystyrene particle in the proposed assay was functionalized with a combination of polyethylene glycol (PEG) spacer terminated with NiNTA and a PEG backfill ligand. The red control particle surface was terminated with PEG only. The PEG groups serve a dual purpose of improving solubility and minimizing non-specific interactions with other particles. The iron oxide particle surface was functionalized with dextran terminated with NiNTA. The dextran serves a similar function as PEG. Future designs will consider the affect of different length PEG spacers and backfill ligands on assay performance.

Particle sizes were chosen based on contact line pinning requirements, settling velocities, and colloid stability (Appendices C, D). Previous studies have shown particles $< 10\mu m$ exhibit the best pinning properties [29]. Polystyrene density of 1.05 g/cm^3 has shown to generate well-defined ring structures. Higher density particles like gold and quantum dots still form rings, but only at small particles sizes, which limit the sensitivity of the assay. A polystyrene diameter of 1μm was chosen based on stability, adequate assay sensitivity and commercial availability. The iron oxide particle diameter of 250nm was chosen after it was observed that 1μm iron oxide particles caused resulted in an unstable colloid causing all particles to fall out of solution (Appendix C).

Poly-l-histidine is a linear peptide polymer consisting of 46 histidine residues (MW 7.9kDa). Nickel requires two adjacent histidine residues for binding, therefore a poly-l-

histidine molecule has approximately 23 nickel binding sites. Histidine rich protein (*pfHRP2*) is a 67kDa protein that consists of 34% histidine assembled in multiple repeats of AHH and AHHAD. The molecule has 54 histidine-histidine motifs; although due to its globular structure not all histidine repeats would be accessible binding sites in the proposed assay. In this study it is assumed that poly-l-histidine can be used as a *pfHRP2* mimic with similar nickel binding characteristics. However, given the differences in molecular size and structure, the proposed assay would likely exhibit a different limit of detection for *pfHRP2*. Samples of *pfHRP2* were not readily accessible for this study resulting in the need to use PLH as a mimic. Other *pfHRP2* mimics exist and should be used in subsequent studies to evaluate assay performance. BNT I and II are peptide dendrimers that have been designed to mimic *pfHRP2* [35]. BNTII is an 8.2kDa molecule with 16 histidine-histidine motifs [35].

Drop size is a basic design parameter having significant influence over assay performance in terms of time and visual appearance. Total evaporation time scales with drop volume (Appendix A) and therefore drop volume dictates how long the assay takes. For all experiments we used 3 µL drops because this volume was the maximum size viewable under a 1.0x objective lens. The drops took approximately 15-25min to dry depending on ambient humidity. Shorter the time-to-answer is preferred; although the smaller the drop size the more difficult it is to visually detect. Ring width scales proportionately with drop volume for a given particle concentration. Deegan empirically demonstrated that ring width scales linearly with drop radius for a given initial particle concentration and follows the functional form $w = aR$; where w is ring width, a is a constant and R is drop radius [2]. Previous studies [32] have found that drop shape

closely resembles a spherical cap having a volume approximated by Equation 7 implying that drop radius scales with $\sqrt{V}$.

$$V = \frac{\pi h \left(3R^2 + h^2\right)}{6} \qquad\qquad (7)$$

Therefore the ideal drop size represents a trade-off between evaporation time, ring width, and overall size (detectability). Moreover, the smaller the drop size the more challenging it will be for an operator to place the drop over a magnetic field with precision and accuracy. Optimal drop size and its impact on assay sensitivity and limit of detection will be the subject of future research studies.

Conclusions and Future Directions

This work has demonstrated a diagnostic assay based on the same mechanism that causes a ring to form in an evaporating coffee drop. This novel method for noninstrumented signal visualization is potentially well-suited for low-resource applications that require a simple-to-use, low cost method for pathogen detection. After exploring and optimizing basic design parameters, we demonstrated proof-of-principle for malaria testing by detecting poly-l-histidine, a biomolecular mimic of *pfHRP2*. The proposed assay was found to have a limit of detection in the mid-nanomolar range, approximately one order of magnitude higher than the clinically relevant range.

Future research will explore ways of lowering the limit of detection to the clinically relevant range, particularly particle surface chemistry, particle size, and particle concentrations.   The work presented uses fluorescent particles in order precisely characterize design particle binding events. However, a field-appropriate device will be

by colorimetric, not fluorescent-based. Adapting the proposed assay to a colorimetric format will be the subject of future engineering efforts. In addition, a device design that is field-appropriate taking into account the need to isolate infected samples and minimize the effect of temperature and humidity on assay performance will be studied in future work.

APPENDIX A

Drop evaporation time

To discern the relationship between drop volume and time required for complete evaporation, 1μm diameter carboxylated polystyrene beads were suspended in deionized water at 1×10^6 particles per μL. Drops of varying volumes were deposited on a plain glass slide in triplicate and the time to complete evaporation measured and recorded. The mean evaporation times are plotted in Figure 16. Error bars represent +/- one standard deviation. The experiment was conducted at room temperature with relative humidity approximately 60%. Observations subsequent to this experiment suggest day-to-day variations in relative humidity can shift the curve up or down by +/- 30%.
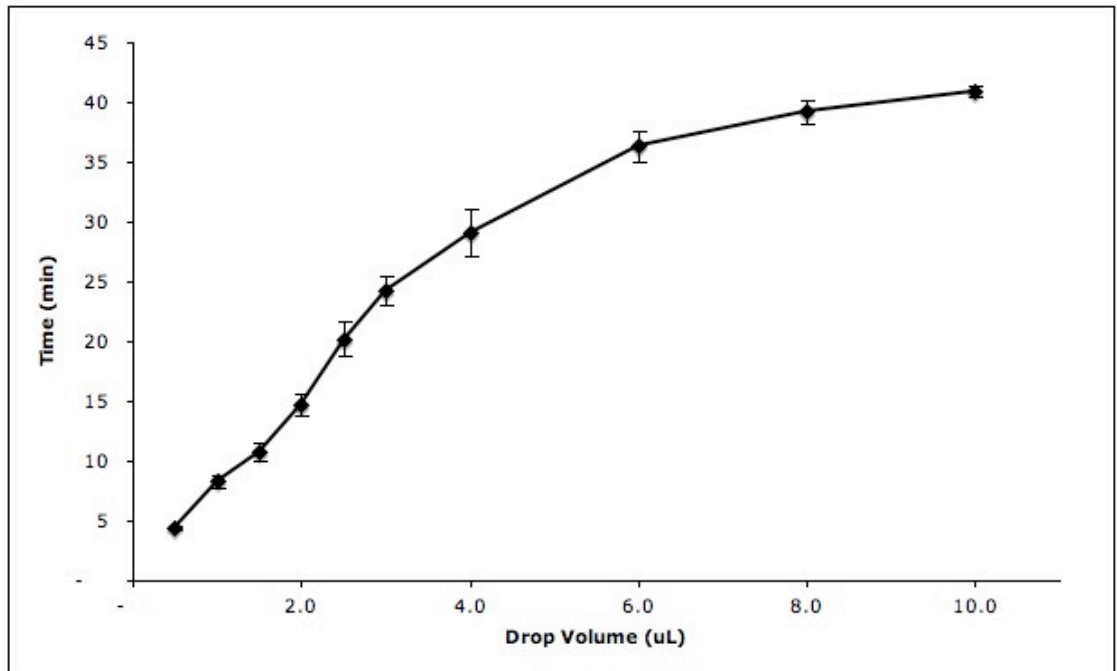

Figure 16. Drop volume-dependent evaporation time.

APPENDIX B

Matlab Ring Simulations

Determining the particle concentration necessary to detect ring formation following drop

evaporation is a key design parameter. A Matlab computer simulation was created to

emulate the evaporation of a drying drop with and without the "coffee ring" formation

that occurs during the evaporation of a solution containing small particles. The

simulation is capable of plotting a range of particle concentrations.

The simulations were all based on the figure above taken of a 1uL drop of PS-COOH

microspheres ($1*10^5$ particles per uL) using a 2x objective lens and a 2 second exposure

time. The diameter of the drop was 2075 um. Using the count function in Image Pro

Plus, the mean area of the visible florescence emitted by one particle was determined to

be 20um. Thus the mean diameter of one particle was determined to be 5 um. The

measurement tool was used to determine that the particles flow to the outer 3% of the

drop's radius.

Using these values the ratio of drop size to fluorescent particle was determined to be

406.86:1. It was determined that one dot is the smallest marker size available on Matlab

for plotting functions and that a dot is equal to 1/72 inch. If the particle size is 1/72 inch,

then the simulated drop size would need to be approximately 5.6 inches in order to

preserve the ratio of 406:1.
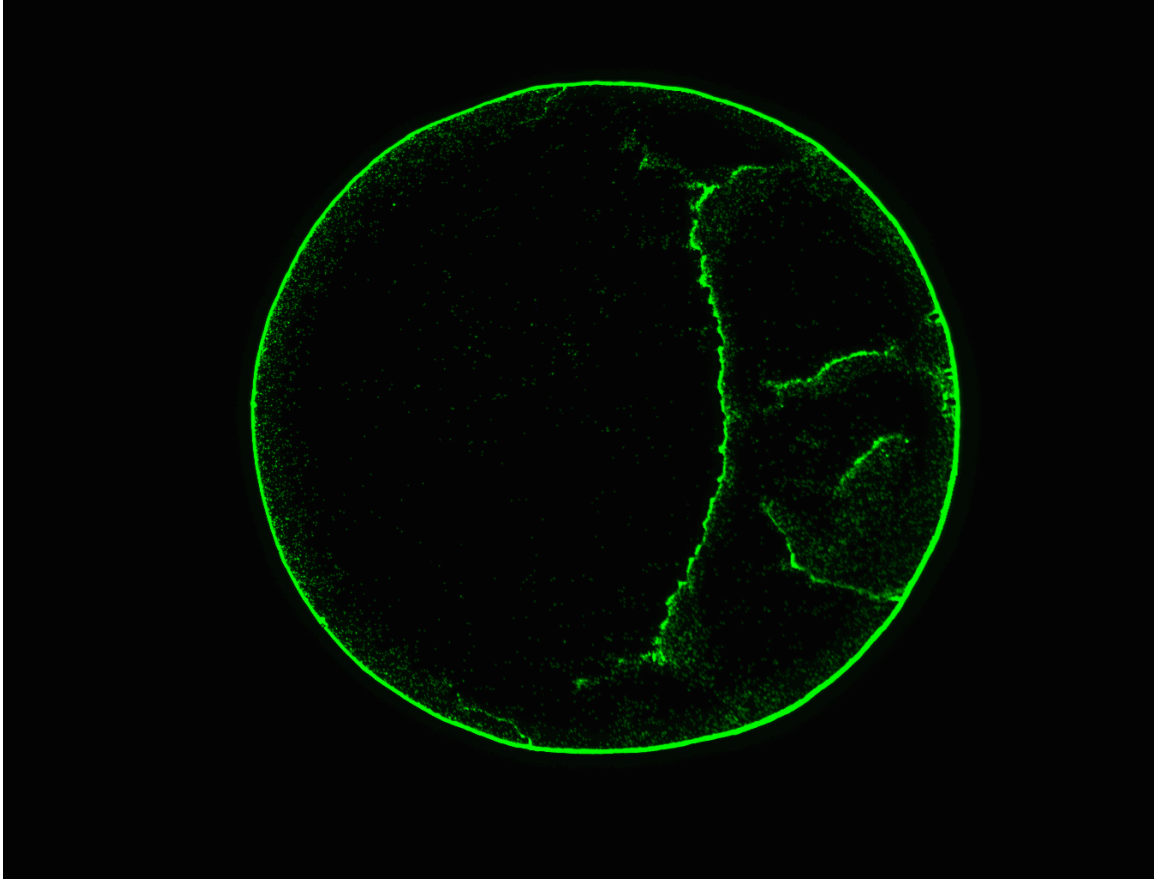
Figure 17: Fluorescence image taken of a 1uL drop of 1μm polystyrene microspheres at $1*10^5$ particles per uL.
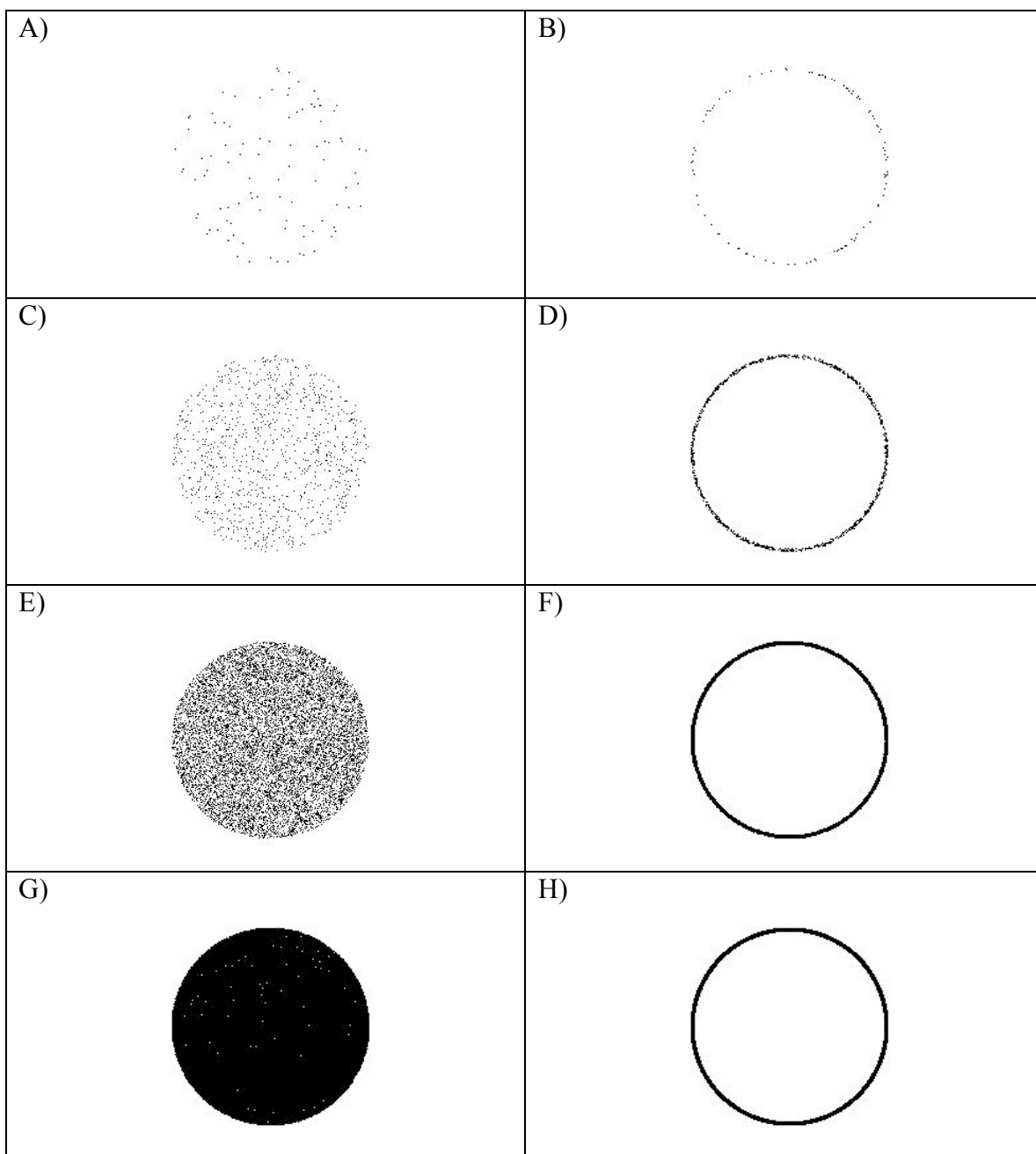
Table 1: Simulations of randomly distributed particles without radial flow (left column) and with radial flow to the outer 3% of the radius (right column). A and B are plots of 100 particles. C and D are plots of 1,000 particles. E and F are plot of 10,000 particles. G and H are plots of 100,000 particles. Images are not scaled such that dots and drop areas correspond to fluorescence data.

Figure 18: 100 randomly distributed particles without radial flow. The ratio of drop size to particle size is approximately 406:1.

Figure 19: 100 randomly distributed particles with radial flow to the outer 3% of the radius. The ratio of drop size to particle size is approximately 406:1
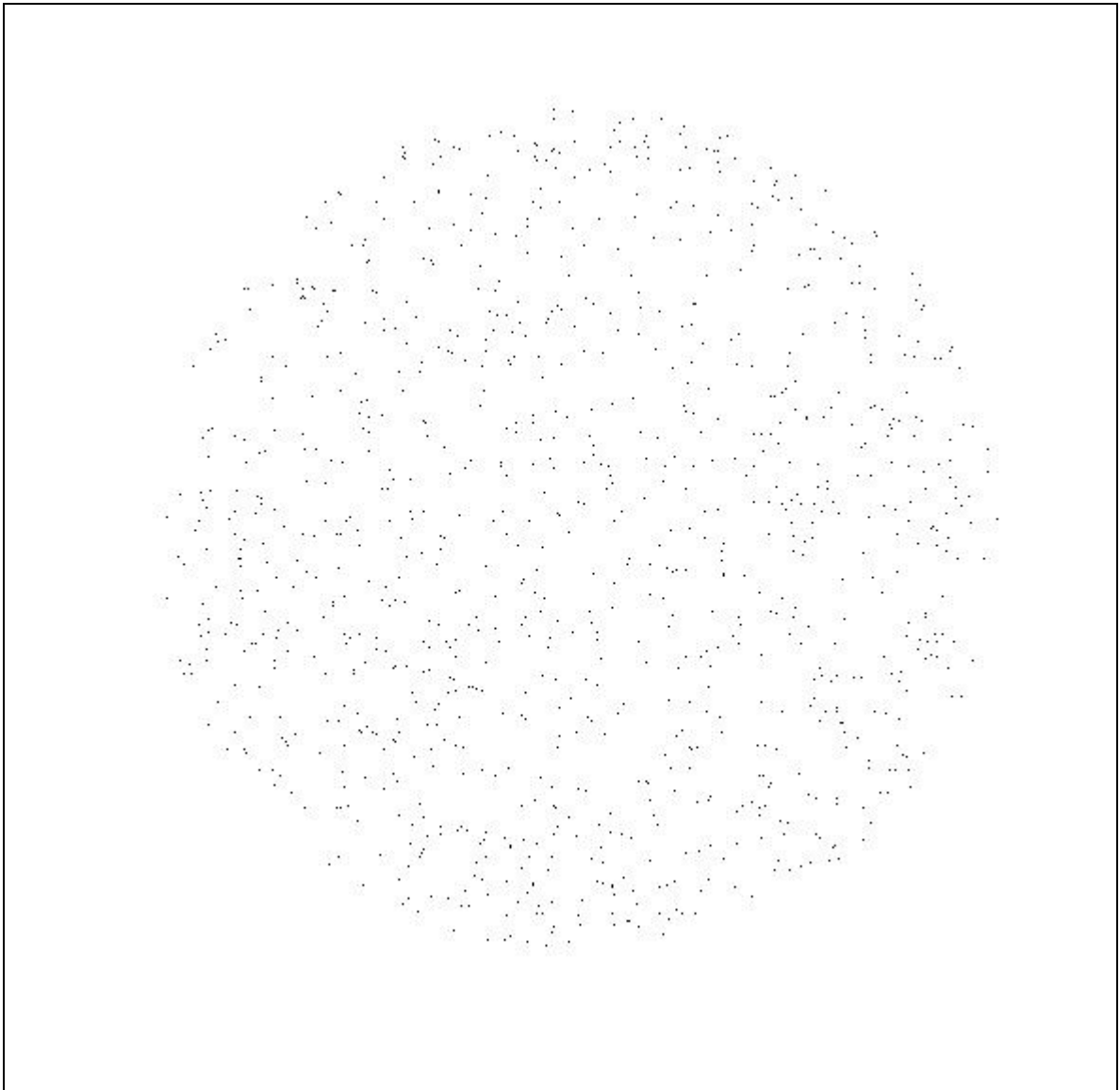
Figure 20: 1000 randomly distributed particles without radial flow. The ratio of drop size to particle size is approximately 406:1
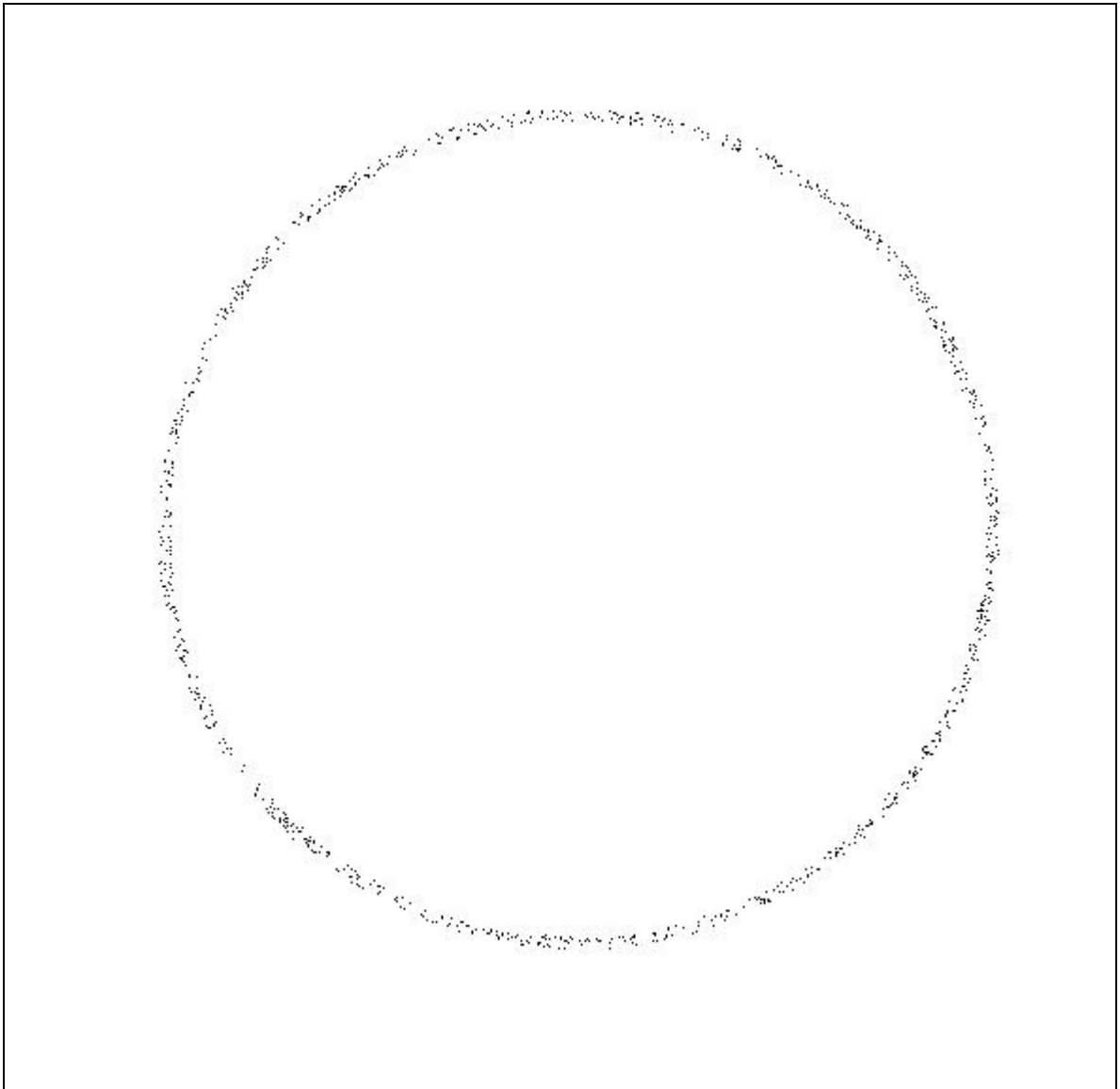
Figure 21: 1000 randomly distributed particles with radial flow to the outer 3% of the radius. The ratio of drop size to particle size is approximately 406:1
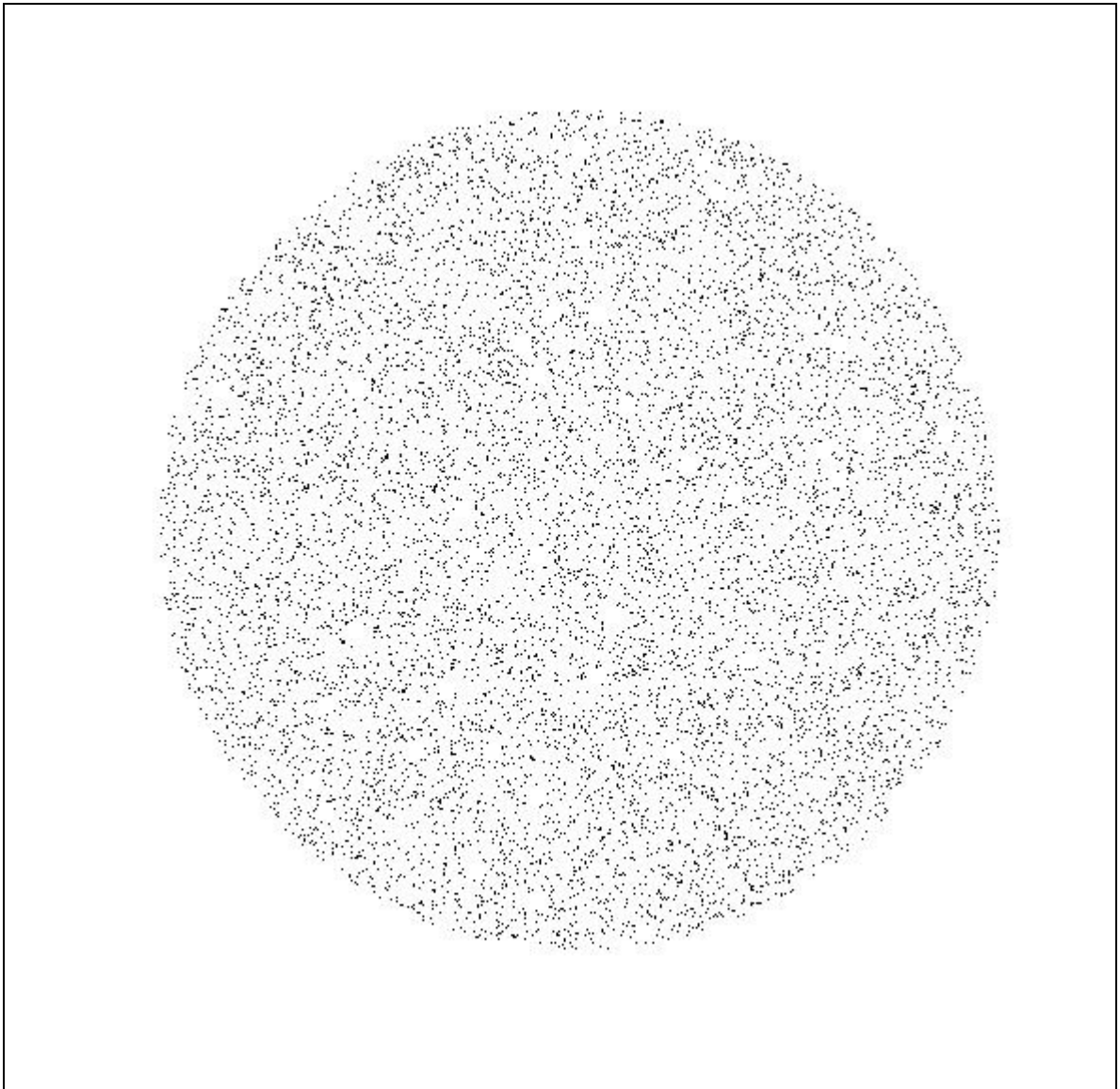
Figure 22: 10,000 randomly distributed particles without radial flow. The ratio of drop size to particle size is approximately 406:1

Figure 23: 10,000 randomly distributed particles with radial flow to the outer 3% of the radius. The ratio of drop size to particle size is approximately 406:1
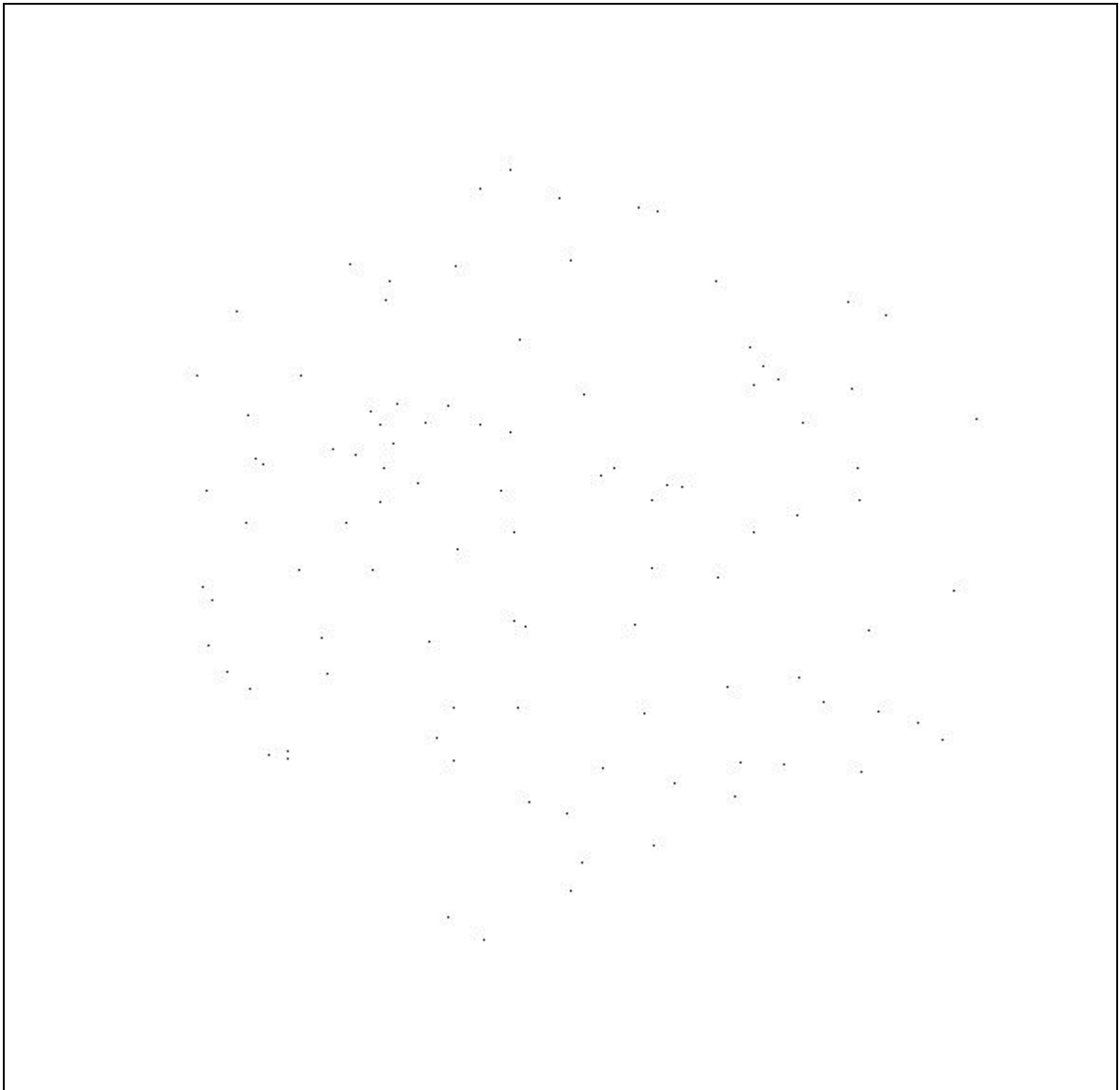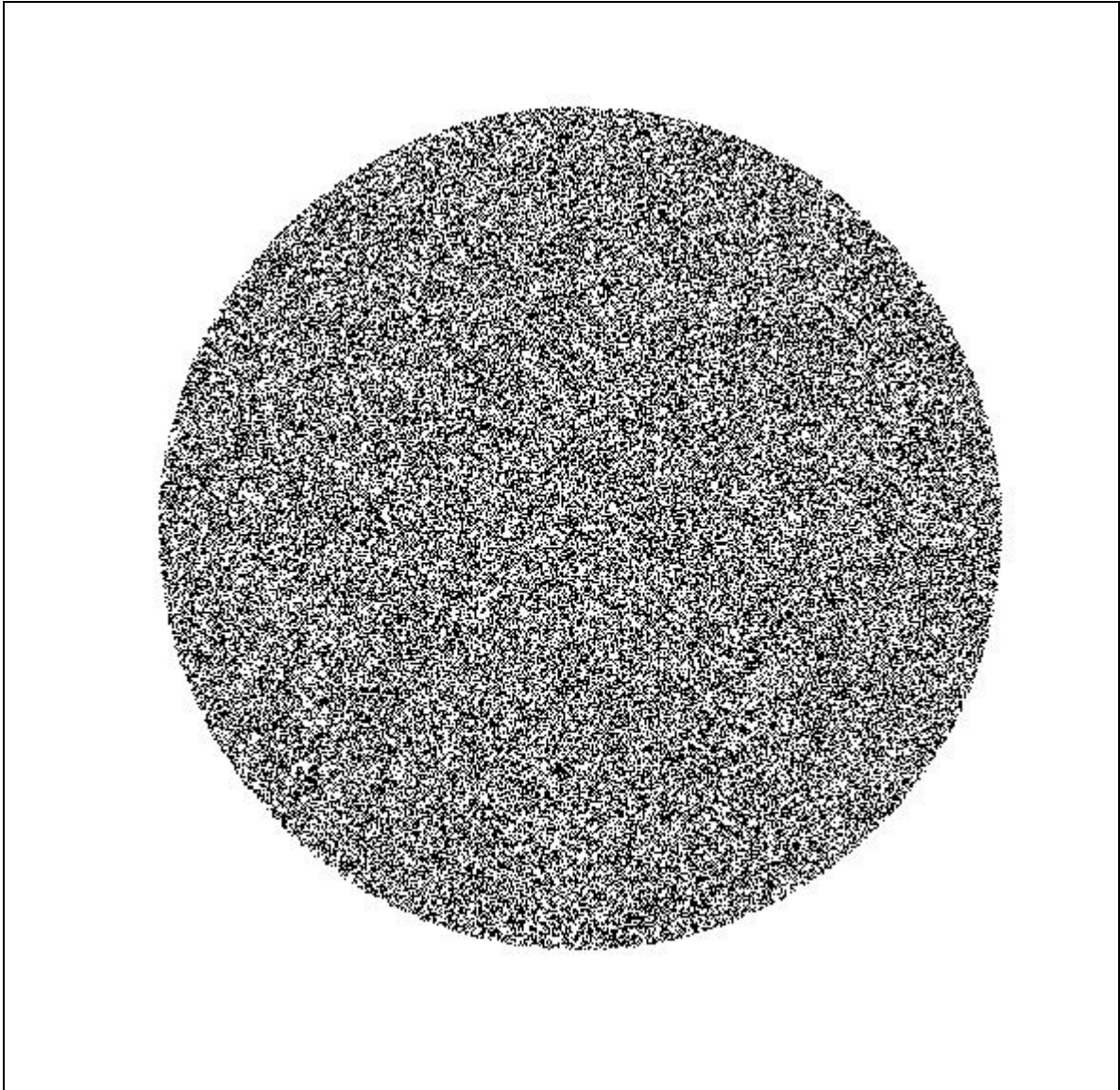
Figure 24: 100,000 randomly distributed particles without radial flow. The ratio of drop size to particle size is approximately 406:1
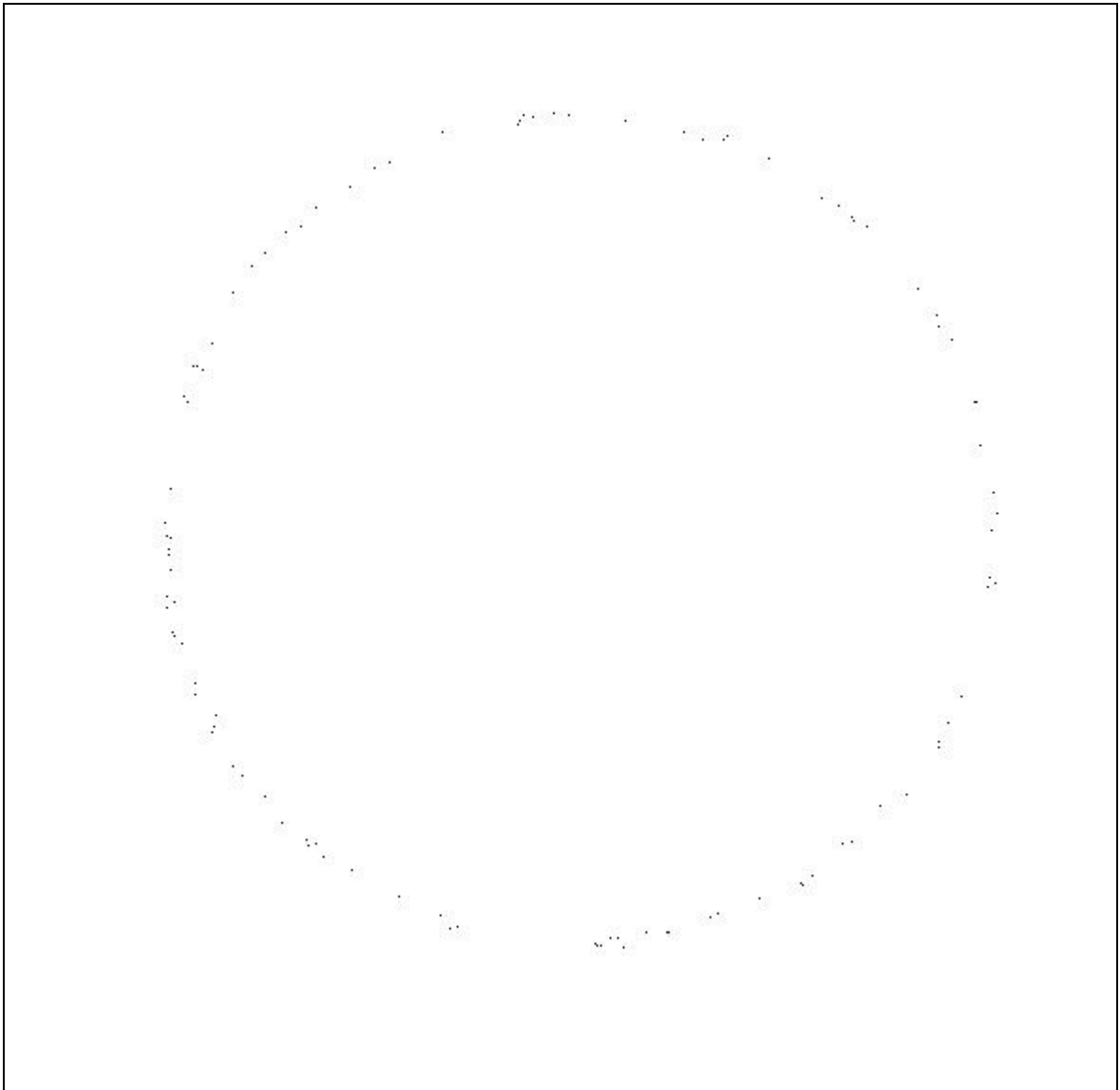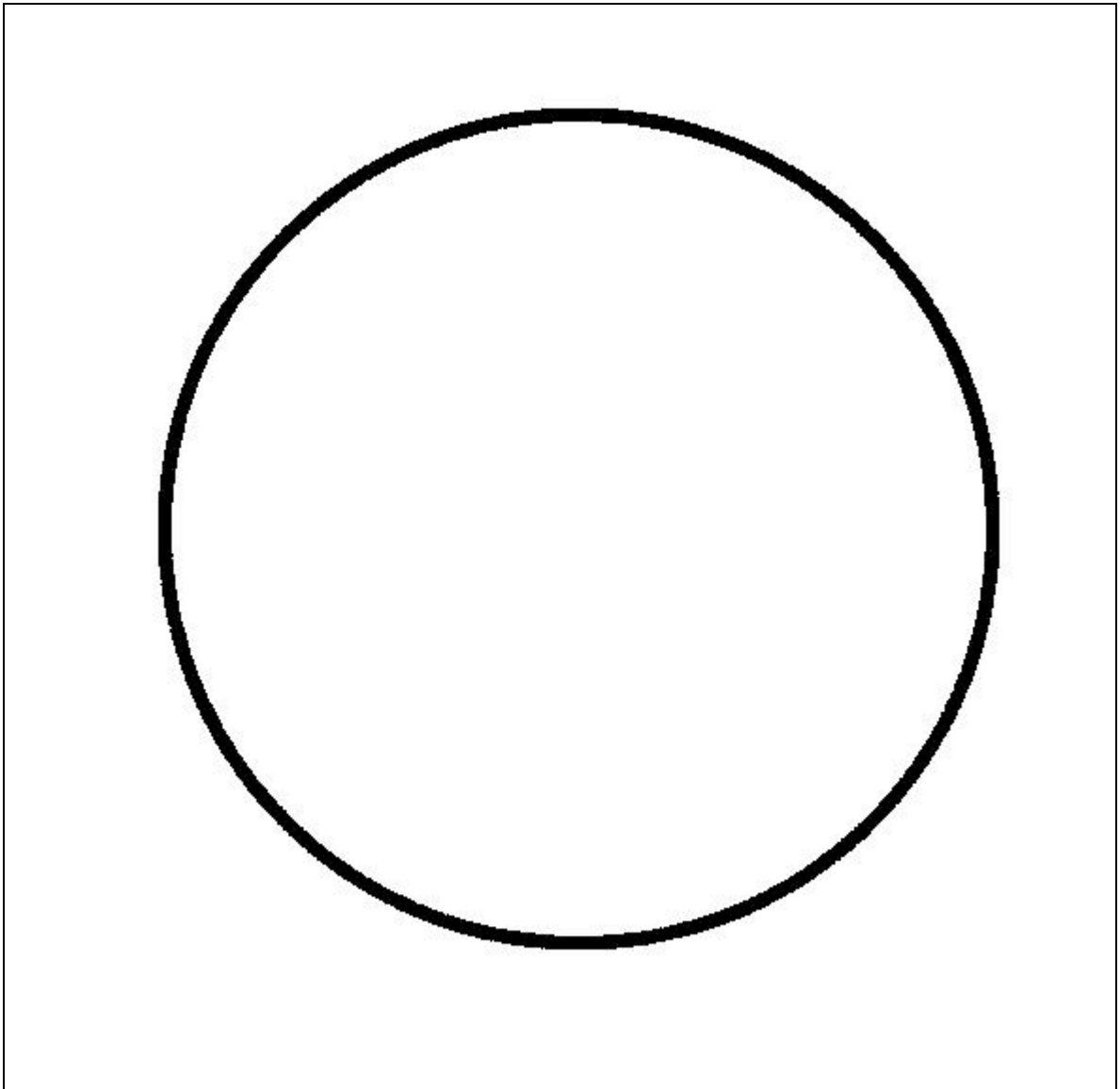
Figure 25: 100,000 randomly distributed particles with radial flow to the outer 3% of the radius. The ratio of drop size to particle size is approximately 406:1
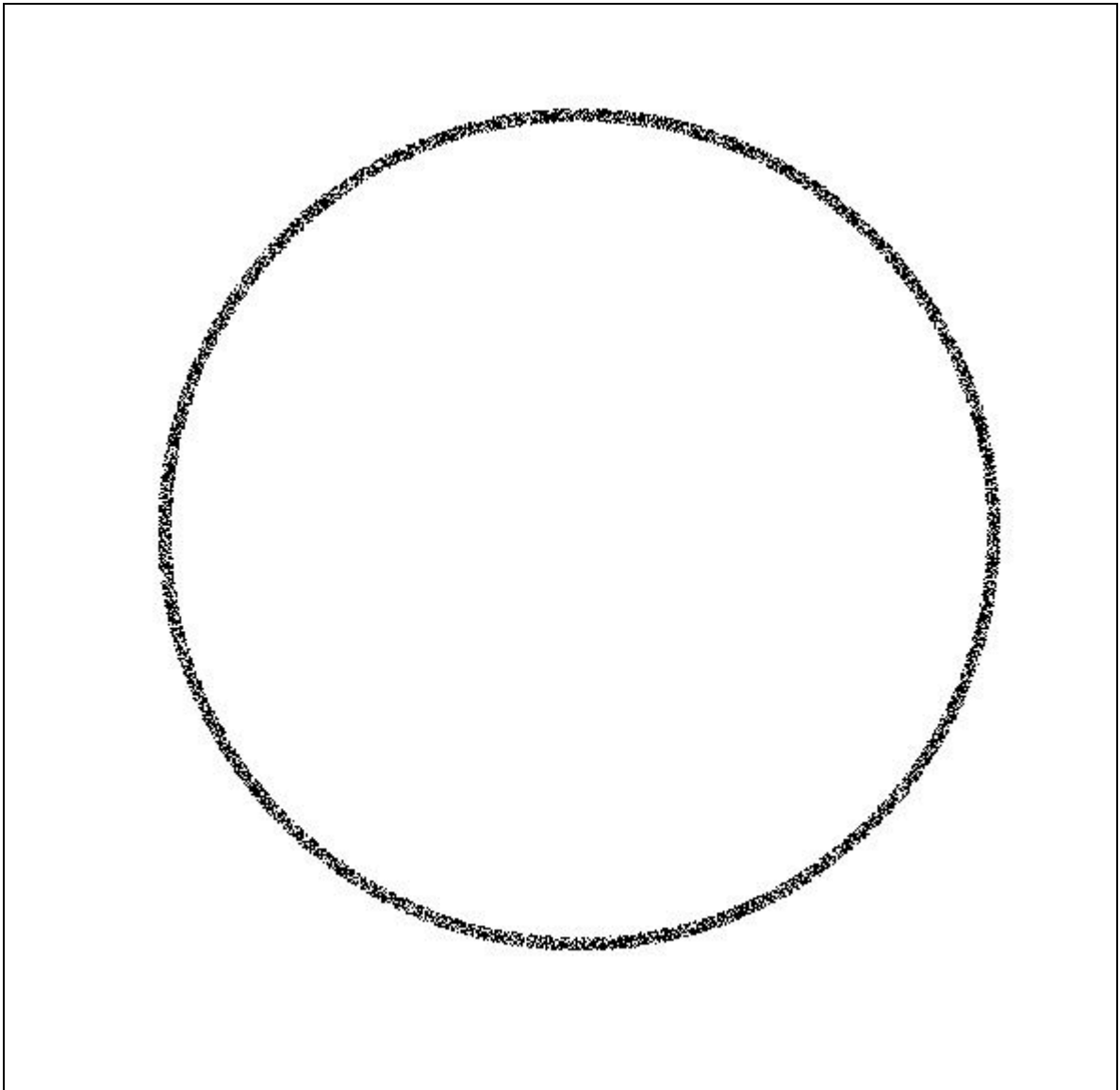
```
%Goal- To create a disk of 100-100,000 randomly distributed points
(without radial flow)

%get rid of everything in memory that could slow it down from previous
stuff
clear all; close all; clc

%assign variable a starting value for while loop
ii=1;

%specify the amount of particles to be plotted (input from user)
particles=input('Number of Particles?'  )

%creates 2 empty matrices for the x and y coordinates of each particle
X=zeros(1,particles);
Y=zeros(1,particles);

%while loop continues until total amount of particles has been generated
while ii<=particles

    %create random x and y coordinate values between -1 and 1
    x=rand(1,1)*-2+1;
    y=rand(1,1)*-2+1;

    %Only plots values that lie within a circle of radius 1
if 1>=sqrt(x^2 + y^2)


    %IF statement is true then:
    %put the values in the matrixes created in lines 17 and 18
    X(1,ii)=x;
    Y(1,ii)=y;

    %and move on to the next particle number
    ii=ii+1;

%if the values do not lie within the circle of radius one, generate new x
%and y values for that same particle
else ii=ii;
end
end

%After while loop has sorting total particle amount in matrices, plot the
%matrices.  Small marker size b/c 1um particles compared to 2mm-3mm drop
plot(X,Y,'o','MarkerFaceColor','k','MarkerEdgeColor','k','markersize',1);
axis square
axis off
```

Figure 26: Matlab code for the simulation of an evaporated drop without radial flow of the particles

```
%Goal-To create a ring of 100-100,000 randomly distributed points to
%represent 1um particles affected by radial flow.
%warning: it may take up to 30sec to plot 100,000 particles
%clears all variables
clear all; close all; clc


%sets a starting point for while loop
ii=1;


%specify the amount of particles to be plotted (input from user)
particles=input('Number of Particles?'  )


%creates 2 empty matrices for the x and y coordinates of each particle
X=zeros(1,particles);
Y=zeros(1,particles);


%while loop continues until total amount of particles has been
generated
while ii<=particles

    %creates a random x and y value in between 1 and -1
    x=rand(1,1)*-2+1;
    y=rand(1,1)*-2+1;

    %use a double true statement so that the coordinates must be in a
    %circle of radius 1 and also must be located on the outer 3% of the
    %edge.
if 1>=sqrt(x^2 + y^2) && .97<=sqrt(x^2 + y^2)
    %IF statement is true then:
    %put the values in the matrixes created in lines 17 and 18
    X(1,ii)=x;
    Y(1,ii)=y;
    %and move on to the next particle number
    ii=ii+1;

    %IF statement is false: stay on same particle number and do while
loop
    %again
else ii=ii;
end
end
%After while loop has sorting total particle amount in matrices, plot
the matrices.  Small marker size b/c 1um particles compared to 2mm-3mm
drop
plot(X,Y,'o',
'MarkerFaceColor','k','MarkerEdgeColor','k','MarkerSize',1);
    axis square
    axis off
```

Figure 27: Matlab code for the simulation of an evaporated drop with radial flow of the particles to the outer 3% of the radius.

APPENDIX C

Iron oxide particle size determination

Several different size iron oxide particles were evaluated for use in the three-particle
assay: 20nm, 100nm, 250nm, and 1.5μm diameter. The 20nm and 100nm were
dismissed as options when it was determined their magnetophoretic mobility was much
too low to be used in an evaporating drop. Particles ≤ 100nm diameter do not exhibit
sufficient superparamagnetism to fall out of solution within the time it takes a drop of
solution to evaporate over a magnetic field (~ 15min for 3μL). The 1.5μm particle
destabilized the colloid causing all particles to fall out of solution during the incubation
step. The 250nm sized particle exhibited sufficient magnetophoretic mobility and
stability and was therefore chosen for use in the proposed assay. To evaluate the
aggregation characteristics using the 1μm iron oxide particle, the following experiment
was performed.

- In a 96-well plate, mix 30 μL of 1μm PS-NiNTA (Micromod Gmbh, p/n 01-48-
  103) and 30μL of silica magnetic-NiNTA (Micromod Gmbh, p/n 39-48-153)
  particles at varying ratios. Incubate two hours.

- Dilute 30μL of sample into 10mL Isoton II solution. (Note: at higher
  concentrations, mix 20μL or 10μL of sample with Isoton II solution).

- Count particles using the Beckman Coulter Multisizer 3 coulter counter with a
  100μm aperture.

- # of particles >5μm was recorded at each particle ratio. The system limit of
  detection was determined to be 1.9μm.

- Each value is the average of three runs, 500μL per run.

[Si, /uL]:	[PS, /uL]: 1E+06	5E+05	1E+05	5E+04	1E+04
1E+04	201	35	18	18	287
5E+04	1,910	985	86	40	11
1E+05	2,200	1,470	469	203	26
5E+05	1,500	1,810	1,490	457	80
1E+06	3,846	7,290	2,260	837	305

Table 2. Aggregates formed when 1.5um silica-iron oxide particles are mixed with 1um polystyrene particles.

Particle Type	Manufacturer	Part Number	Color, Fluor Y/N	Surface Chemistry	Stock Concentration (particles/mL)	Diameter (um)	Density (g/cm³)	Settling Velocity (µm/s)
Polystyrene	Bangs Labs	FC03F/9927	Green, Y	-cooh	1.98E+10	0.970	1.05	0.02561
Polystyrene	Bangs Labs	FC03F/9803	Red, Y	-cooh	1.98E+10	0.970	1.05	0.02561
Polystyrene	Micromod	01-48-103	White, N	-NiNTA	9.30E+10	1.000	1.05	0.02722
Silica-iron oxide	Micromod	39-48-153	Brown, N	-NiNTA	5.66E+09	1.500	2.50	1.83750
Iron oxide	Micromod	09-11-252	Brown, N	-NTA	4.90E+11	0.250	2.50	0.05104
Iron oxide	Micromod	79-02-102	Brown, N	-cooh	7.50E+12	0.100	1.40	0.00218
Iron oxide	Micromod	79-02-201	Brown, N	-cooh	8.00E+14	0.020	1.40	0.00009
Gold	BBI / Tedpella	15714-20	Pink, N	N/A	3.60E+08	0.250	19.30	0.62271
Quantum Dot	Invitrogen		Red, Y	-cooh	4.82E+12	0.015	8.00	0.00086

[1] Assuming aqueous solution having density = 1.0 g/cm³; viscosity = .001 Pa*s

Table 3. Particle Data.

APPENDIX E

Zeta potentials

Chemical groups present on a particle surface dictate electrostatic charge on the surface and how the particle interacts with an ionic solution. These characteristics are therefore expected to change upon surface modification. Zeta potential is a measure of particle electrophoretic mobility between two electrodes across which a constant voltage is applied. We measured zeta potential before and after particle surface modification as a means of verification. Zeta potentials were measured using a Malvern Zetasizer.

Particle	Average Zeta Potential (mV)	Standard Deviation
80% PEG NiNTA	-27.3	0.586
50% PEG NiNTA	-30.2	0.751
30% PEG NiNTA (11/10/10)	-24.5	0.721
10% PEG NiNTA	-23.6	0.907
mPEG (11/19/10)	-17.5	0.52
COOH	-43.1	0.085

Table 4. Particle zeta potentials before and after functionalization.

Effect of particle concentrations on SNR: multivariate regression model

A regression analysis was performed with signal-to-noise as the dependent variable and PS-NiNTA concentration and iron oxide-NiNTA concentration as the independent variables. The analysis of variance suggests SNR is positively and statistically affected by a change in PS-NiNTA concentration.

Multiple R	0.70
R Square	0.49
Adjusted R Square	0.42
Standard Error	0.53
Observations	25

Table 6. Regression statistics.

	[PS-NiNTA]	[FeOx-NiNTA]
Coefficients	0.43	(0.03)
Standard Error	0.12	0.06
t Stat	3.55	(0.51)
P-value	0.00	0.61
Lower 95%	0.18	(0.16)
Upper 95%	0.69	0.10
Lower 95.0%	0.18	(0.16)
Upper 95.0%	0.69	0.10

Table 6. Analysis of variance

Figure/Table	Description	File Name(s)
Figure 3	Assay schematic	10 Dec 8_assay schematic.jpg
Figure 4	Particle chemistry	
Upper panel	3 particles	10 Dec 8_Individual particles_revised.jpg
Middle panel	Cross-linking	10 Dec 8_Particles.bmp
Middle panel	Cross-linking	10 Dec 8_HRP.bmp
Middle panel	Cross-linking	10 Dec 8_Particles plus HRP.bmp
Lower panel	NiNTA chemistry	10 Dec 8_NiNTA_v2.bmp
Figure 5	Magnet-slide evaporation apparatus	10 Dec 8_experimental setup_cropped.jpg
Figure 6	Areas of interest for intensity measurements	10 Dec 8_AOI figure.ppt
Figure 7	Number of 1um particles needed to form a ring	10 Dec 1_varying [PS]_tiled2.jpg
Figure 8	Varying NiNTA surface coverage: effect on signal in 2-particle assay	10 Nov 13_Varying NiNTA coverage_tiled.jpg
Figure 9	SNR in 2-particle assay with varying NiNTA surface coverage	10 Nov 13_exp2_data.xls
Figure 10	SNR in 2-particle assay with varying [PS-PEG-NiNTA] and [FeOx-NiNTA]	10 Nov 19_data.xls
Figure 11	Order of addition	10 Nov 15_Order of addition_tile.jpg
Figure 12	3-particle assay: positive vs negative	10 Nov 24_A19c-A20c_tiled2.jpg
Figure 13	Limit of detection panel	10 Nov 24_LOD panel_tiled.jpg
Figure 14	Limit of detection: SNR	10 Nov 24_LOD data_final.xls
Figure 15	Limit of detection: ring color	10 Nov 24_LOD data_final.xls
Figure 16	Appendix A: Evaporation time vs drop volume	10 Sep 30_Drying times of PS in H2O.xls
Figure 17; Table 1; Figures 18-27	Appendix B: Matlab drop simulation	10 Dec 3_Matlab_Simulation.doc
Table 2	Appendix C: Aggregate data mixing 1um PS-NiNTA with 1.5um Si-Feox-NiNTA	10 Sep 8_Coulter Counter_PS-NiNTA+Si-NiNTA.xls
Table 3	Appendix D: Particle data table	10 Dec 8_particle table.xlsx
Table 4	Appendix E: Zeta potential data table	10 Dec 8_Bead Zeta.xls
Table 5	Appendix F: Regression statistics	10 Nov 19_data.xls
Table 6	Appendix F: Analysis of variance	10 Nov 19_data.xls
Table 7	Appendix G: Data cross-reference	10 Dec 8_data cross reference.xls

Table 7. Data cross-reference.

REFERENCES

1.   Ngom, B., et al., *Development and application of lateral flow test strip technology for detection of infectious agents and chemical contaminants: a review.* Analytical and Bioanalytical Chemistry, 2010. **397**(3): p. 1113-1135.

2.   Deegan, R.D., *Pattern formation in drying drops.* Physical Review E, 2000. **61**(1): p. 475-485.

3.   Malkin, R.A., *Design of health care technologies for the developing world.* Annu Rev Biomed Eng, 2007. **9**: p. 567-87.

4.   *Global Burden of Disease.* 2009; Available from: http://www.globalburden.org/GBD_Study_Operations_Manual_Jan_20_2009.pdf.

5.   *Global Health Facts.* Available from: www.globalhealthfacts.org.

6.   Yager, P., G.J. Domingo, and J. Gerdes, *Point-of-care diagnostics for global health.* Annu Rev Biomed Eng, 2008. **10**: p. 107-44.

7.   *Malaria : evaluation of rapid diagnostic tests.* 2009.

8.   Bell, D. and World Health Organization. Regional Office for the Western Pacific., *The use of malaria rapid diagnostic tests.* 2nd ed. 2006, Geneva: World Health Organization. 19 p.

9.   Wongsrichanalai, C., et al., *A review of malaria diagnostic tools: Microscopy and rapid diagnostic test (RDT).* American Journal of Tropical Medicine and Hygiene, 2007. **77**(6): p. 119-127.

10.   World Health Organization. Regional Office for the Western Pacific., *Malaria rapid diagnosis: making it work : informal consultation on field trials and quality assurance on malaria rapid diagnostic tests : meeting report 20-23 January 2003.* 2003, Manila: WHO Regional Office for the Western Pacific. 61 p.

11.   *WHO World Malaria Report.* 2008.

12.   *World Health Organization Malaria Fact Sheet.* Available from: www.who.int/mediacentre/factsheets/fs094/en/.

13.   Bloland, P.B. *Drug resistance in malaria.* 2001; Available from: www.cdc.gov/malaria/pdf/bloland_WHO2001.pdf.

14.   Nosten, F. and P. Brasseur, *Combination therapy for malaria: the way forward?* Drugs, 2002. **62**(9): p. 1315-29.

15. Gay, F., et al., *Direct acridine orange fluorescence examination of blood slides compared to current techniques for malaria diagnosis.* Transactions of the Royal Society of Tropical Medicine and Hygiene, 1996. **90**(5): p. 516-518.

16. Cooke, A.H., et al., *Use of the Fluorochrome Benzothiocarboxypurine in Malaria Diagnosis.* Transactions of the Royal Society of Tropical Medicine and Hygiene, 1992. **86**(4): p. 378-378.

17. Sharma, M.K., et al., *Highly sensitive amperometric immunosensor for detection of Plasmodium falciparum histidine-rich protein 2 in serum of humans with malaria: comparison with a commercial kit.* Journal of Clinical Microbiology, 2008. **46**(11): p. 3759-65.

18. Singh, N. and N. Valecha, *Evaluation of a rapid diagnostic test, 'Determine malaria pf', in epidemic-prone, forest villages of central India (Madhya Pradesh).* Ann Trop Med Parasitol, 2000. **94**(5): p. 421-7.

19. Reyburn, H., et al., *Rapid diagnostic tests compared with malaria microscopy for guiding outpatient treatment of febrile illness in Tanzania: randomised trial.* BMJ, 2007. **334**(7590): p. 403.

20. Ochola, L.B., et al., *The reliability of diagnostic techniques in the diagnosis and management of malaria in the absence of a gold standard.* Lancet Infect Dis, 2006. **6**(9): p. 582-8.

21. Baker, J., et al., *Genetic diversity of Plasmodium falciparum histidine-rich protein 2 (PfHRP2) and its effect on the performance of PfHRP2-based rapid diagnostic tests.* J Infect Dis, 2005. **192**(5): p. 870-7.

22. Murray, C.K. and J.W. Bennett, *Rapid Diagnosis of Malaria.* Interdiscip Perspect Infect Dis, 2009. **2009**: p. 415953.

23. Piper, R., et al., *Immunocapture diagnostic assays for malaria using Plasmodium lactate dehydrogenase (pLDH).* American Journal of Tropical Medicine and Hygiene, 1999. **60**(1): p. 109-18.

24. Bustos DG, O.R., Negishi M, Kurimura T., *Evaluation of a new rapid diagnostic test "Determine Malraia Pf" against standard blood film, ICT Malaria P. f and ParaSight F.* Japanese J. Trop. Med. & Hyg., 1999. **27**(3): p. 417-425.

25. Bell, D. and R.W. Peeling, *Evaluation of rapid diagnostic tests: malaria.* Nat Rev Microbiol, 2006. **4**(9 Suppl): p. S34-8.

26. WHO, *World Malaria Report.* 2008.

27. Deegan, R.D., et al., *Capillary flow as the cause of ring stains from dried liquid drops.* Nature, 1997. **389**(6653): p. 827-829.

28. Deegan, R.D., et al., *Contact line deposits in an evaporating drop.* Physical Review E, 2000. **62**(1): p. 756-765.

29. Sangani, A.S., et al., *Capillary force on particles near a drop edge resting on a substrate and a criterion for contact line pinning.* Physical Review E, 2009. **80**(1): p. -.

30. Hu, H. and R.G. Larson, *Evaporation of a sessile droplet on a substrate.* Journal of Physical Chemistry B, 2002. **106**(6): p. 1334-1344.

31. Hu, H. and R.G. Larson, *Analysis of the microfluid flow in an evaporating sessile droplet.* Langmuir, 2005. **21**(9): p. 3963-3971.

32. Kajiya, T., D. Kaneko, and M. Doi, *Dynamical Visualization of "Coffee Stain Phenomenon" in Droplets of Polymer Solution via Fluorescent Microscopy.* Langmuir, 2008. **24**(21): p. 12369-12374.

33. Ausubel, F.M., *Short protocols in molecular biology : a compendium of methods from Current protocols in molecular biology.* 5th ed. 2002, New York: Wiley. 2 v. (various pagings).

34. Derjaguin, B.L., L, *Theory of the stability of strongly charged lyophobic sols and the adhesion of strongly charged particles in solutions of electrolytes.* Acta Physico Chemica URSS, 1941. **14**(633).

35. Ziegler, J., R.T. Chang, and D.W. Wright, *Multiple-antigenic peptides of histidine-rich protein II of Plasmodium falciparum: Dendrimeric biomineralization templates.* Journal of the American Chemical Society, 1999. **121**(11): p. 2395-2400.